A Simplified Serotonin Neuron Model

Emerson Harkin

Thesis submitted to the
Faculty of Graduate and Postdoctoral Studies
in partial fullfillment of the requirements
for the Master's degree in Neuroscience

Supervisor: Dr. Jean-Claude Béïque
Co-supervisor: Dr. Richard Naud

Department of Cellular & Molecular Medicine
Faculty of Medicine
University of Ottawa

Abstract

The serotonin (5HT) neurons of the dorsal raphe nucleus (DRN) play an important and nuanced role in regulating animal behaviour. They exhibit heterogenous and dynamic responses to rewards and punishments *in vivo*, and perturbations of their activity modulate diverse behavioural states. This functional complexity is reflected in the network architecture of the DRN, with its multiple cell types, local feed-forward and recurrent connections, and partially segregated input-output streams that span most of the forebrain. At the centre of this elaborate circuit, 5HT neurons themselves are now believed to be highly electrophysiologically heterogenous. As a first step towards leveraging these observations to better understand the role of the DRN in regulating behaviour, we set out to produce a phenomenological 5HT neuron model capable of bridging the gap between single-neuron dynamics and network processing. We found that a class of leaky integrate-and-fire (LIF)-derived models that accurately replicate the firing behaviour of a variety of cortical neuron types could not capture the behaviour of 5HT neurons. This is because, unlike cortical pyramidal neurons, 5HT neurons exhibit pronounced nonlinearities in their subthreshold dynamics near action potential threshold due to a pair of voltage-dependent potassium currents operating on distinct timescales. Augmenting the LIF-derived model with both potassium currents resulted in a significantly improved description of 5HT neuron firing dynamics. Additionally, we report that the distributions of the biophysical parameters that describe these potassium currents and other fundamental properties of 5HT neurons suggest the existence of a single, highly variable underlying population of these cells, rather than multiple distinct serotonergic types. Our simplified 5HT neuron model opens the door to understanding how the essential biophysical features of these cells and their cell-to-cell variability shape population-level encoding of behavioural variables in the DRN.

Acknowledgements

First and foremost, I would like to thank my supervisor, Dr. Jean-Claude Béïque, and co-supervisor, Dr. Richard Naud, for their guidance, mentorship, and encouragement. The intellectually stimulating environment they have created has helped me improve the quality of my research, learn to communicate my work to a variety of audiences, and obtain funding—all of which are of course essential to science.

This project has been a team effort and would not have been possible without the work of a great number of talented people. Along with Dr. Béïque and Dr. Naud, Michael Lynn, Dr. Alexandre Payeur, and Dr. André Longtin formed an interdisciplinary partnership that laid the foundation for the work presented here. Their insight continues to be very valuable as we work towards extending these results. I would also like to thank David Lemellin, Liwen Cai, and Dr. Ginette Hupé for technical assistance and input on the project.

I first met my thesis advisory committee members, Dr. Mario Tiberi and Dr. Paul Albert, when I began my time in Dr. Albert's lab as an honours student three years ago. Over the years, their feedback has been a valuable source of insight that has helped me continually improve my work.

I would also like to thank my evaluators, Dr. Leonard Maler and Dr. Tuan Bui, for taking the time to read and assess my thesis.

I would like to thank Michael Lynn, Sébastien Maillé, Sean Geddes, Philippe Vincent-Lamarré, Dr. Cary Soares, and all the members of the Béïque, Naud, and Bergeron groups for helpful discussions and for having made the lab a great place to be over the past two years.

Finally, I would like to thank my family and my partner, Rachel Urban Shipley, for all their support... and for letting me go on about raphe projections late into the evening.

Contents

List of figures

List of tables

List of abbreviations

4AP 4-aminopyridine

5CT 5-carboxamidotryptamine

5HT serotonin

ACSF artificial cerebrospinal fluid

AHP after-hyperpolarization

BNST bed nucleus of the stria terminalis

CeA central amygdala

DRN dorsal raphe nucleus

vmDRN ventromedial dorsal raphe nucleus

GIF generalized integrate-and-fire

KGIF K-augmented generalized integrate-and-fire

ISI inter-spike-interval

LIF leaky integrate-and-fire

LNP linear-nonlinear poisson model

LTP long-term potentiation

mPFC medial prefrontal cortex

MSE mean squared error

OLS ordinary least-squares

OUN Ornstein-Uhlenbeck noise

SERT serotonin transporter

STDP spike time dependent plasticity

TEA tetraethylammonium

TPH tryptophan para-hydroxylase

TTX tetrodotoxin

VTA ventral tegmental area

1 Introduction

1.1 Role of the DRN in regulating behavioural states

The forebrain-projecting serotonin neurons of the dorsal raphe nucleus (DRN) play a key role in regulating appropriate behavioural responses to a changing environment, but the precise nature of this role is not well understood. This small population of neurons has received a great deal of attention for its involvement in supporting adaptive behavioural responses to stress in animal models [1], modulating internal mood-states in humans [2], and mediating the therapeutic effects of widely-used antidepressant medications [3, 4]. In contrast to the dopaminergic neurons of the ventral tegmental area, where a large body of work detailing the involvement of this population in reward-seeking behaviour has led to a unifying theoretical framework describing the mapping between a specific behavioural variable (i.e., reward prediction error) and the firing patterns of these cells [5], a unified theory of the coding properties of DRN serotonin neurons has remained elusive [6].

The coding properties of serotonin neurons have been particularly difficult to explain due in part to their complex and heterogenous responses to emotionally-salient stimuli. Investigations using a fluometric approach to record DRN 5HT population activity have reported that 5HT neurons respond phasically to rewarding stimuli [7] and gradually develop an anticipatory activity ramp as animals learn to associate reward-predicting cues with unconditioned rewards [8]. There has been conflicting evidence as to whether 5HT neurons respond to aversive as well as rewarding stimuli (reviewed in [9]). Whereas 5HT neurons have been reported not to respond to aversive stimuli at the population level [7], investigations using an *in vivo* electrophysiological approach to record from individual neurons have observed both reward- and punishment-sensitive cells [10, 11]. Very recent work has resolved some of these apparent discrepancies by providing strong evidence that the DRN contains segregated ensembles of 5HT neurons that differ in terms of their responsiveness to aversive stimuli and long-range

connectivity [12]. To summarize, DRN 5HT neurons exhibit heterogenous responses to both the delivery and anticipation of aversive and/or appetitive environmental stimuli which vary over time and across DRN subregions. It is no wonder that a concise interpretation of this non-stationary, non-uniform observational data has not appeared.

A small number of groups have attempted to clarify the role of 5HT neurons by optogenetically manipulating their activity during behaviour. Converging lines of evidence from this body of work suggest an important role for serotonin in supporting sustained reward-directed actions. Specifically, stimulation of DRN 5HT neurons appears to promote 'patient' waiting for reward [13–15]. Remarkably, although activation of 5HT cells promotes a type of reward-seeking behaviour and even modulates the rate of reward learning [16], stimulation of 5HT neurons does not appear to be directly reinforcing [13, 14, 16, 17] (but see [18]). An important limitation of these experiments is that the passive waiting behaviour that 5HT neuron stimulation promotes may be confounded with a more generalized reduction in locomotor activity [12, 17]. However, a recent report that stimulation also promotes active waiting (i.e., repeated nose-poking) supports the existence of a direct effect on reward-seeking behaviour [19].

The literature on the role of the DRN along other behavioural dimensions is less cohesive, largely due to methodological differences. In particular, the impact of optogenetic stimulation on behavioural responses to aversive stimuli and general locomotor activity depends heavily on which subset(s) of DRN neurons are targeted. Activation of the DRN as a whole (including non-5HT neurons) promotes escape behaviour in animals subjected to an uncontrollable stressor and increases locomotor activity [1], while phasic stimulation of DRN 5HT neurons transiently decreases locomotor activity without impacting behavioural measures of anxiety [17], and activation of a projection-defined subset of DRN 5HT neurons increases anxiety-like behaviour without impacting locomotor activity [20]. Others have noted similarly disparate findings across studies using a broader range of methodologies [12].

Clearly, the 5HT neurons of the DRN play key roles in regulating animal behaviour. Their

spontaneous activity tracks emotionally-salient environmental stimuli, and perturbations in their activity modulate behavioural responses to appetitive and aversive cues. However, far from establishing a cohesive account of the behavioural and environmental variables encoded by the DRN, recent work has instead highlighted the multifaceted nature of its behavioural role [12]. So far, the coding scheme of the DRN defies simple explanations [6].

1.2 Anatomy and physiology of the DRN network

The apparent complexity of the serotonergic code is matched by the complexity of the network architecture of the DRN. To provide a basis for beginning to understand the origin of the heterogenous activity of 5HT neurons during behaviour, this section will review the anatomy and physiology of the DRN with emphasis on recent evidence of its heterogenous structure.

1.2.1 Physiology of DRN serotonin neurons

The rodent brain contains approximately 26000 serotonin neurons [21], so named for their ability to synthesize 5-hydroxytryptamine (5HT) from the essential amino acid tryptophan. Of these, approximately 12000 to 15000 have their cell-bodies located in the DRN [21, 22]. This group projects widely throughout the central nervous system, and is the main source of serotonergic input to the forebrain [23, 24]. These cells exhibit a characteristic morphology with a small (diameter $\sim$18 µm in rat), ovoid cell soma, few primary dendrites, and little dendritic arborization [22, 25]. The axonal systems of serotonin neurons are highly collateralized, and single neurons have been reported to innervate multiple downstream regions [26]. Vesicular release of serotonin occurs at varicosities and terminals throughout the axonal system, following which the serotonin is taken back up via the serotonin transporter (SERT) (a sodium- and chloride-dependent cotransporter [27]) and recycled.

DRN 5HT neurons receive direct, excitatory input from principal neurons throughout much of the forebrain (reviewed in detail in section 1.2.3) as well as local inhibitory input.

Based on rabies-tracing experiments, 5HT neurons receive local input from GABA cells and other 5HT neurons in roughly equal proportion [28]. The GABAergic input mediates feed-forward inhibition by long-range inputs [29], and the serotonergic input has been suggested to mediate recurrent inhibition within the DRN network [30].

DRN serotonin neurons were long thought to be fairly uniform in terms of their electrophysiological features. Pioneering work on this system suggested that serotonin neurons could be distinguished from other cell types in the DRN by their characteristic slow, regular firing *in vitro* and *in vivo*, high membrane resistance, and expression of $5\,HT_{1A}$ receptors [31–33]. While these are important characteristics of a large fraction of 5HT neurons, more recent work has shown that 5HT neurons cannot be reliably differentiated from other cell types in the DRN based on any of these features [10, 25], partly because 5HT neurons are more electrophysiologically-heterogenous than previously believed [25, 34, 35]. In light of these new developments, a model-based understanding of the properties of positively-identified 5HT neurons that explicitly accounts for this observed cell-to-cell heterogeneity is needed to provide insight into how the DRN network supports the heterogenous coding scheme observed *in vivo*.

1.2.2 Physiology of other DRN cell-types

Along with 5HT neurons, the DRN contains a significant population of GABAergic cells, and smaller numbers of glutamatergic and dopaminergic cells about which little is known. The DRN GABAergic population shows almost no overlap with the 5HT neuron population [36, 37], and can itself be subdivided into a large group of somatostatin-expressing cells located mainly in the lateral wings of the DRN [36, 38–41], along with a very small group of VIP-expressing cells clustered around the lower half of the aqueduct [42, 43]. Only a minority of experimental studies differentiate between subtypes of GABAergic neurons in the DRN, and it is not known whether these populations differ in their electrophysiological properties. DRN GABA neurons are largely similar to serotonin neurons in terms of their

passive electrophysiological properties, but exhibit a fast-spiking phenotype [44]. Eventually, it will be necessary to construct a single-neuron model of DRN GABA cells in order to understand how local interactions between 5HT and GABA neurons shape the network dynamics of the DRN (underway but outside the scope of this report).

1.2.3 Long-range connectivity

DRN serotonin neurons provide dense and highly divergent input to nearly every forebrain region. The DRN provides direct input to regions involved in regulating behavioural responses to rewarding and aversive stimuli (e.g., orbitofrontal and infralimbic cortices, amygdala, bed nucleus of the stria terminalis, and lateral habenula) as well as regions responsible for sensory processing and movement [24]. Several groups have observed some degree of spatial segregation of 5HT neurons within the DRN with respect to their target regions [45–48], with one very recent investigation providing strong evidence for largely segregated cortical- and subcortical-projecting serotonergic ensembles located in the ventromedial and dorsolateral DRN, respectively [12]. The cortical-projecting population of 5HT neurons located in the ventromedial DRN is particularly notable because of its high proportion of VGLUT3 co-expressing cells [12, 26, 37].

Non-serotonergic DRN neurons also contribute to this region's long-range outputs. The DRN sends a direct, behaviourally reinforcing input to the ventral tegmental area (VTA) that consists mainly of strictly glutamatergic neurons (46 %) along with smaller numbers of neurons that co-express tryptophan para-hydroxylase (TPH), strictly serotonergic neurons, and unidentified cells [49]. DRN GABAergic neurons have also been reported to make long-range connections with the olfactory bulb and the bed nucleus of the stria terminalis (BNST) [41, 43].

The DRN receives direct forebrain input from a wide range of forebrain and brainstem regions that is anatomically segregated and organized according to target cell-type. According to whole-brain rabies-tracing experiments, DRN neurons receive most of their input from

the amygdala, hypothalamus, and brainstem, with less input from various cortical regions (mainly motor and orbitofrontal cortices) and the lateral habenula [28, 50, 51], although this approach does not necessarily reflect functional connectivity (see [52]). DRN 5HT and GABA neurons appear to differ mainly in terms of their input from cortex and the central amygdala (CeA), with 5HT neurons receiving proportionately more cortical input while GABAergic cells receive more input from CeA (which is itself mainly GABAergic, and therefore disinhibitory) [28, 53]. In general, inputs to 5HT neurons from CeA appear to be more concentrated in the dorsolateral DRN compared with cortical inputs, which preferentially target the ventromedial DRN [12].

The input structure of the DRN is not static over time. Using an *in vitro* electrophysiological approach, our group has shown that endocannabinoid signalling differentially regulates the strength of descending medial prefrontal cortex (mPFC) inputs on 5HT and GABA neurons [29], and that glutamatergic synapses on 5HT cells are transiently weakened by chronic antidepressant treatment [54]. These observations illustrate that endogenous mechanisms as well as environmental factors can regulate the network architecture of the DRN.

1.3 Towards a model-based understanding of DRN function

The anatomy and physiology of the DRN necessarily shape its function. Recent work has shown that the DRN network is more complex than previously believed in terms of its cellular architecture, local circuitry, and the organization of its long-range connections. A model-based framework for understanding the DRN could leverage these observations to determine what computations this network architecture might support, ultimately shedding light on how 5HT neurons regulate behaviour. In this section we discuss the first step towards a DRN network model: a simplified model 5HT neuron.

A 5HT neuron model well suited to bridging the gap between single neuron behaviour and network dynamics has not yet been described. A model ideally suited to making this connection must strike a compromise between biophysical detail and computational simplic-

ity, but existing models of 5HT neurons sit at opposite ends of this spectrum (see [55] for an excellent review). Previous models are either only loosely constrained to experimental data (achieving similar firing rates but not necessarily reproducing other features of excitability) [56, 57], or are tightly constrained but too complex to be suitable for network simulations [58]. In addition, previous work does not explicitly account for the observed heterogeneity among 5HT neurons. In the electrosensory system of the weakly electric fish *Apteronotus leptorhynchus*, neural heterogeneity implements a population-level redundancy-reduction mechanism, considerably increasing the information density of population codes for sensory stimuli [59]. In the DRN, heterogeneity among individual 5HT neurons may have a similar role, facilitating efficient encoding of behavioural variables at the network level. The goal of this project is therefore to address the limitations of previous work by creating a 5HT model that contains only a minimal set of biophysically meaningful parameters that are tightly constrained to experimental data and that reflect the underlying heterogeneity of the 5HT neuron population.

Generalized integrate-and-fire (GIF) neuron models are ideally suited to bridging the gap between the biophysical basis of neural integration and network dynamics. The construction of the GIF is rooted in the work of Louis Lapicque, who first observed over 100 years ago that the electrotonic properties of neuronal membranes were well approximated by those of a leaky capacitor, forming an RC circuit between the inside and outside of the cell [60] (republished in English as [61]). This observation is the foundation of widely-used leaky integrate-and-fire (LIF) models, which impose a hard voltage threshold at which spikes occur over the leaky integrator activity described by Lapicque. Rather than a hard threshold, the GIF extends the simple RC circuit model of neuronal subthreshold dynamics with a stochastic spiking rule taken from linear-nonlinear poisson models (LNPs). LNPs describe neurons in terms of a set of arbitrarily-shaped linear input filters (which might describe, in a *statistical* sense, how the activity of the neuron is correlated with its input, spike history, or even the activity of neighbouring neurons; see [62] for a notable example of the use of a generalized

version of LNPs to understand how spatially correlated population activity encodes sensory information in the visual system) coupled to the rate of a spike-generating non-stationary Poisson process via some nonlinear function [63, 64]. If an exponential function is used for the nonlinear coupling, the likelihood of obtaining an observed spike train becomes a concave function of the linear input filter coefficients [63]. This convenient property means that LNPs can very easily be tuned to optimally reproduce spiketrains from experimental data via maximum likelihood estimation of the input filters [63, 64]. The GIF takes advantage of this property to find a soft voltage threshold that best explains an observed set of spikes from an individual neuron, given the subthreshold dynamics estimated by the RC circuit model [65].

By combining the minimal biophysical constraints of an RC circuit model of subthreshold dynamics with the stochastic spiking framework of LNPs, the GIF presents a simplified biophysical model of the integrative features of single neurons that can easily be constrained to experimental data [65]. While the GIF lacks part of the biological realism of biophysically detailed conductance-based models (the GIF does not describe the ionic currents that lead to action potentials, nor the activity of any voltage-gated ion channel), it is able to capture the behaviour of real neurons surprisingly well, predicting the spiketrains of cortical pyramidal neurons with millisecond precision [65–67]. Because the GIF is expressed in terms of biophysical parameters (unlike LNPs), it is more easily extended to account for the effects of specific biophysical phenomena (e.g. nonlinearities introduced by voltage-gated ion channels, or changes in the shape of the after-hyperpolarization (AHP)) on the spiketrains to which it is constrained. Finally, the biophysical parameterization of the GIF adds little computational overhead compared with LNPs widely used for network modelling. Together, these characteristics make the GIF an excellent tool for our eventual goal of understanding how the integrative features of 5HT neurons shape DRN network dynamics.

1.4 Summary

The complex network architecture of the DRN supports its nuanced and important role in regulating animal behaviour. However, the details of how behavioural and environmental variables are internally represented in the DRN remain unclear. In order to move towards a unified understanding the behavioural role of the DRN, we set out to create a fundamental building block of an experimentally-grounded DRN network model: a simplified 5HT neuron model. Our goal was to create a model that accounts for the most important biophysical processes that regulate firing in 5HT neurons, while remaining compact enough for network simulations. The GIF is a biophysically-constrained version of the LNPs widely used in network modelling that has been reported to predict the spiketrains of cortical pyramidal neurons with millisecond precision [65–67]. However, in our hands, the GIF much more poorly reflected the firing behaviour of DRN 5HT neurons than mPFC L5 pyramidal cells. Using the GIF as a starting point for our modelling efforts, we first identified two phenomenological voltage-dependent potassium currents that contribute to the poor performance of the GIF in 5HT cells. Next, by characterizing these two currents and incorporating them into the GIF, we created a new potassium-augmented GIF model that better captures the firing behaviour of 5HT neurons. Finally, we discuss the implications of our model for understanding the general processing features of 5HT neurons, sources of functional heterogeneity in this population, and potential consequences for some aspects of network-level processing.

2 Materials and methods

2.1 Experimental procedures

2.1.1 Animals

Experiments were performed on male and female C57/Bl6 mice aged 4-8 weeks expressing the fluorescent marker TdTomato under the control of the SERT promoter. Animals were group-housed and kept on a 12:12-h light/dark cycle with access to food and water *ad libidum*. All experiments were carried out in accordance with procedures approved by the University of Ottawa Animal Care and Veterinary Services.

2.1.2 Slice preparation

Animals were deeply anaesthetized using isofluorane (Baxter Corporation) before being euthanized by decapitation. The brain was quickly removed from the skull into ice-cold choline dissection buffer containing the following: 119.0 mM choline chloride, 2.5 mM KCl, 4.3 mM $MgSO_4$, 1.0 mM $CaCl_2$, 1.0 mM NaH_2PO_4, 1.3 mM Na ascorbate, 11.0 mM glucose, 26.2 mM $NaHCO_3$; saturated with 95 % O_2/5 % CO_2. A Leica VT1000S vibratome was used to cut 300 µm sections of the DRN in the same ice-cold choline dissection buffer. After cutting, slices were placed in a recovery chamber filled with standard artificial cerebrospinal fluid (ACSF) containing the following: 119.0 mM NaCl, 2.5 mM KCl, 1.3 mM $MgSO_4$, 2.5 mM $CaCl_2$, 1.0 mM NaH_2PO_4, 11.0 mM glucose, 26.2 mM $NaHCO_3$; ∼298 mOsm, maintained at 37 °C, and continuously bubbled with 95 % O_2/5 % CO_2. The recovery chamber was allowed to equilibrate to room temperature for 1 h before beginning recording.

2.1.3 *In vitro* whole-cell electrophysiological recording

DRN neurons were visualized using an upright microscope (Olympus BX51WI) equipped with differential interference contrast and a 40×, 0.8 NA water-immersion objective. Whole-

cell recordings were obtained from fluorescently-labelled 5HT neurons using glass electrodes (Sutter Instruments; tip resistance 4–6 MΩ) containing K-gluconate-based internal solution (135 mM K gluconate, 6.98 mM KCl, 10 mM HEPES, 4 mM Mg ATP, 0.40 mM GTP, 10 mM Na phosphocreatine; adjusted to pH 7.25 with KOH, 280–290 mOsm). For voltage clamp experiments, whole-cell capacitance compensation was applied manually following break-in. All experiments were carried out at room temperature. Neurons with access resistance >30 MΩ or unstable holding current at −70 mV were excluded from analysis. Recordings were collected with an Axon MultiClamp 700B amplifier, filtered at 2 kHz, and digitized at 10 kHz using an Axon Digidata 1550 digitizer.

2.2 Computational methods

2.2.1 Leaky integrate-and-fire model

The simplest model used in this work is the LIF neuron model. The LIF neuron consists of an RC-circuit model of neuronal subthreshold dynamics coupled with a hard voltage threshold at which the neuron emits a spike. The subthreshold dynamics of the LIF neuron are given by

$$C\frac{dV}{dt} = -g_l(V(t) - E_l) + I(t) \tag{1}$$

where C is the membrane capacitance, $g_l = 1/R_m$ is the leak conductance (R_m is the membrane resistance), E_l is the equilibrium potential of the leak conductance (equivalent to the resting membrane potential in this case), and $I(t)$ is the time-varying input current. When the voltage of the neuron reaches a threshold value $\theta = -45$ mV the model emits a spike and the voltage is reset to a lower value $V_{\text{reset}} = -60$ mV.

The subthreshold part of the LIF model can be further simplified by expressing time in units of the membrane time constant and expressing the input stimulus relative to the leak

conductance. The subthreshold dynamics given in eqn. 1 then simplify to

$$\frac{dV}{dt'} = -(V(t') - E_l) + I'(t') \tag{2}$$

where $t' = t/\tau$ and $I'(t) = I(t)/g_l$.

2.2.2 Generalized integrate-and-fire model

The GIF model used as a starting point for a simplified serotonin neuron model is based on the work of Pozzorini *et al.* [65]. Briefly, the GIF is comprised of an RC-circuit model of neuronal subthreshold dynamics and a soft voltage threshold for spiking. The subthreshold dynamics of the GIF neuron are the same as given above in eqn. 1. The GIF neuron emits spikes stochastically according to an inhomogenous Poisson process with a time-varying rate $\lambda(t)$, given by

$$\lambda(t) = \lambda_{\text{ref}} \exp\left(\frac{V(t) - V_T(t)}{\Delta V}\right) \tag{3}$$

where $V_T(t)$ is the instantaneous spike threshold at time t, ΔV is the threshold width, and λ_{ref} is a reference firing rate to preserve units (arbitrarily fixed at 1 Hz). In discrete time, the probability that n spikes are emitted during a time step of width Δt is given by $P\{N[t, t + \Delta t) = n\} = \frac{\lambda(t)^n}{n!} e^{-\lambda(t)}$. In our work, Δt (0.1 ms) is sufficiently small that at most one spike can be emitted in an individual timestep. The probability of spike emission $P\{N[t, t + \Delta t) = 1\}$ therefore simplifies to

$$P_{\text{spk}}(t) = 1 - e^{-\lambda(t)\Delta t} \tag{4}$$

2.2.3 Models of potassium currents

Ionic conductances in this work are modeled using a simplified Hodgkin-Huxley formalism.

$$I_A(t) = \bar{g}_A m_\infty h(V(t) - E_K) \tag{5}$$

$$I_{\text{Kslow}}(t) = \bar{g}_{\text{Kslow}} n_\infty (V(t) - E_K) \tag{6}$$

where $I_x(t)$ denotes the current passed by conductance x; $\bar{g}_x$ denotes the maximal conductance; E_K is the Nernst reversal potential for potassium ($-101\,\text{mV}$ in this case); and m, h, and n are gating variables. The steady-state voltage-dependence of the gating variables is given by the first order Boltzmann function

$$x_\infty(V) = \frac{A}{1 + \exp(-k(V - V_{1/2}))} \tag{7}$$

where $V_{1/2}$ is the midpoint of the activation function, k is the slope factor, and A is a scaling factor. The time dynamics of the gating variables take the form

$$\frac{dx}{dt} = \frac{x_\infty - x}{\tau_x} \tag{8}$$

2.2.4 Augmented leaky integrate-and-fire model

For simulations involving a simple neuron with I_A, the LIF neuron described above in 2.2.1 was augmented with a variable amount of I_A in the subthreshold dynamics as follows

$$\frac{dV}{dt'} = -(V(t') - E_l) - \bar{g}'_A m_\infty h(V(t') - E_K) + \sigma_{\text{noise}}\xi(t') + I'(t') \tag{9}$$

where $\bar{g}'_A = \bar{g}_A / g_l$ is the effective amount of I_A, and $\xi(t')$ is a random noise term that follows a Gaussian distribution $\mathcal{N}(0, 1)$ with a scaling factor σ_{noise}.

2.2.5 Augmented generalized integrate-and-fire model

Augmented GIF neurons with I_A and/or K_{slow} were constructed by inserting the I_A/K_{slow} dynamics defined in eqns. 5–6 into the subthreshold dynamics of the base GIF (eqn. 1), yielding the following augmented subthreshold models

$$C\frac{dV}{dt} = -g_l(V(t) - E_l) - \bar{g}_A m_\infty h(V(t) - E_K) + I(t) \tag{10}$$

$$C\frac{dV}{dt} = -g_l(V(t) - E_l) - \bar{g}_{\text{Kslow}} n_\infty (V(t) - E_K) + I(t) \tag{11}$$

$$C\frac{dV}{dt} = -g_l(V(t) - E_l) - (\bar{g}_A m_\infty h + \bar{g}_{\text{Kslow}} n_\infty)(V(t) - E_K) + I(t) \tag{12}$$

For all GIF-type neurons, the spiking rule is given by eqn. 4.

2.2.6 Data analysis and numerical methods

Data analysis was carried out using Python 2.7 scripts that were custom written or modified from [65]. The following third-party Python packages were used: `numpy` and `numba` for numerical simulations; `scipy` for statistical analysis and signal processing; and `matplotlib` and `seaborn` for figure creation. Statistical tests are indicated in the text, and non-parametric tests were used when the normality assumption was not warranted.

In all simulations numerical integration was performed according to the Euler-Maruyama method using a timestep of 0.1 ms or $10^{-3}\tau_{\text{mem}}$. In some cases spikes are shown on simulated traces from GIF or LIF neurons for clarity, but their amplitude is meaningless. Simulations were run using Python 2.7 on MacOS or Linux.

3 Results

3.1 Physiology of DRN serotonin neurons

To understand the general integrative features of forebrain-projecting serotonin neurons, we carried out *in vitro* whole-cell electrophysiological recordings of fluorescently-labelled serotonin neurons in the ventromedial DRN. Morphologically, serotonin neurons were characterized by an oval to fusiform soma with a small number of sparsely-ramified primary dendrites (see fig. 1B). In response to step currents, serotonin neurons emitted slow, adapting trains of single spikes (see fig. 1C & S4). When tetrodotoxin (TTX) was used to block voltage-dependent sodium channels, serotonin neurons exhibited large outward currents in response to voltage steps from $-80\,\mathrm{mV}$ to near spike threshold (see fig. 1D). As previously reported, application of 5-carboxamidotryptamine (5CT) elicited a hyperpolarizing current (see fig. 1E), indicating that these neurons express $5\,\mathrm{HT}_{1\mathrm{A}}$ receptors [54]. Finally, we found that serotonin neurons had low leak conductance ($1.03 \pm 0.35\,\mathrm{nS}$; equivalent to a membrane resistance of $1.13 \pm 0.57\,\mathrm{G\Omega}$), small capacitance ($69.7 \pm 16.0\,\mathrm{pF}$), long membrane time constant ($75.5 \pm 29.5\,\mathrm{ms}$), and a resting membrane potential near $-70\,\mathrm{mV}$ ($-68.7 \pm 12.0\,\mathrm{mV}$), all of which except the membrane time constant were normally-distributed (Shapiro W-test $p > 0.05$ in each case, except membrane time constant $\tau = \frac{C_m}{g_l}$; see fig. 1F).

3.2 Validation of GIF model

The GIF is a highly simplified neuron model that can be trained to precisely predict the firing behaviour of individual pyramidal neurons using limited data [65]. The GIF consists of three parts: an RC-circuit model of neuronal subthreshold dynamics (see fig. 2A1), a stochastic spiking mechanism that depends on voltage (see 2A2), and spike-triggered changes to the former two parts. If the spike-triggered phenomena are omitted, the behaviour of the GIF is dictated by only five parameters ($g_l = 1/R_{\mathrm{mem}}$, C, and E_l for the subthreshold part; V_T

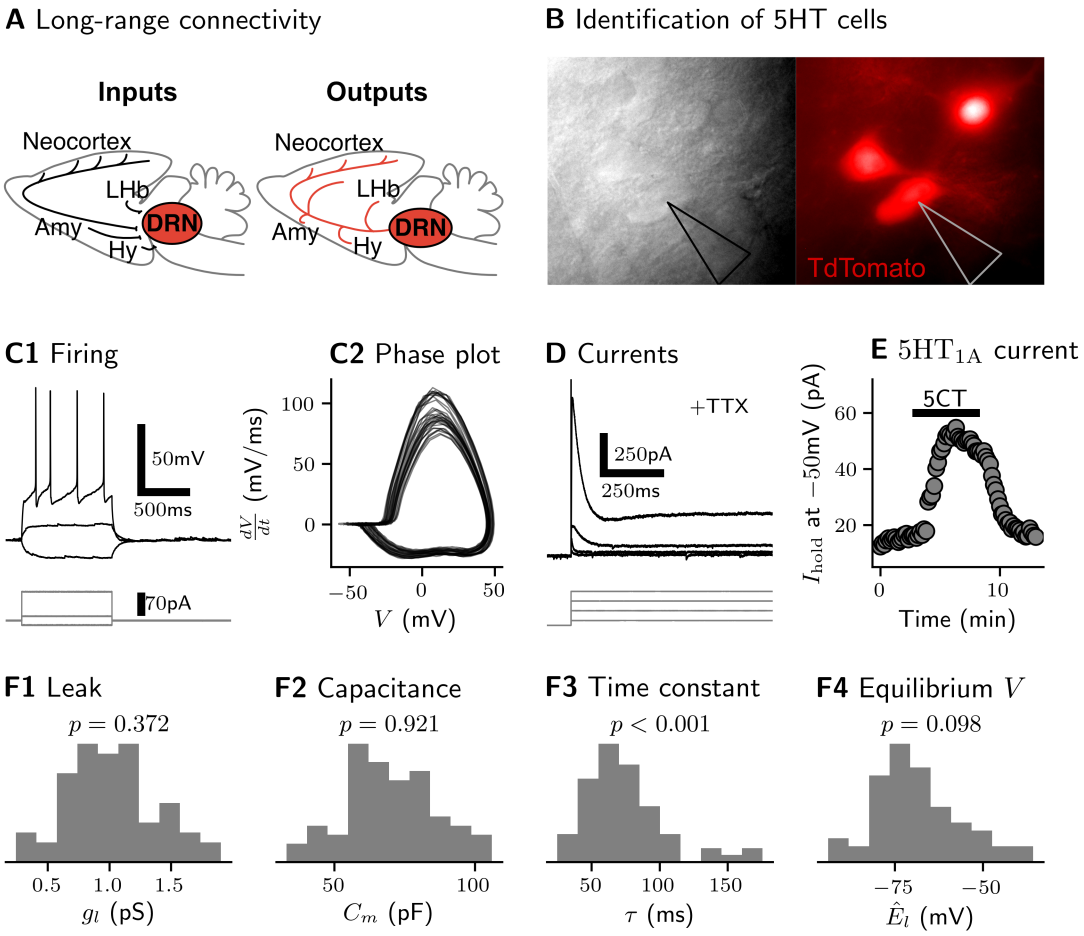

Figure 1: Physiology of serotonin neurons. *A.* Long-range connectivity patterns of DRN 5HT neurons. Amygdala (Amy), hypothalamus (Hy), lateral habenula (LHb). *B.* Identification of 5HT neurons. DIC (left) and fluorescence (right) imaging of DRN 5HT neurons showing Cre-dependent expression of TdTomato. Triangle indicates the location of the patch pipette. *C.* Spiking characteristics. *D.* Whole-cell currents in TTX. *E.* 5HT neurons express $5\,\mathrm{HT}_{1\mathrm{A}}$ receptors. *F.* Passive membrane parameters. p-values are from Shapiro W-tests for normality. $N = 63-64$ cells.

and ΔV for the spiking mechanism). Values for these parameters can be extracted from $\sim$1 min of data recorded from a single neuron in current clamp (see fig. 2B for a typical experiment and fig. 2C for an outline of the fitting procedure), producing a model that has been 'trained' to emulate the behaviour of the neuron to which it was fitted.

To validate the GIF, we stimulated L5 mPFC pyramidal neurons with Ornstein-Uhlenbeck noise (OUN) (a model of synaptic noise) for $\sim$1 min and trained a set of GIF models using this data (termed the training dataset). We then stimulated the same neurons with 10 repetitions of a new 10 s OUN stimulus (termed the test dataset) and compared their responses with the predictions of the GIF. In our hands, the predictions of the GIFs were in close agreement with the responses of the real neurons to the new input (see fig. 2D1 for a representative example). We found that the GIFs accurately predicted the subthreshold response of the neurons to the new input ($R^2 = 0.907 \pm 0.037$, see fig. 2D2). To quantify the performance of the GIFs with respect to spike-timing predictions we used the M_d^* spiketrain similarity metric [68]. M_d^* quantifies the similarity of two sets of spiketrains on a scale from 0 to 1 (larger numbers indicate greater similarity) at a given level of precision (4 ms used here). In this case, we used M_d^* as a measure of the average similarity between the ten test set spiketrains recorded from each mPFC neuron and a set of 500 spiketrains realized from the corresponding model. Because the test dataset contains multiple replicates of the same test stimulus, the value of M_d^* is partially corrected for the intrinsic unreliability of the neuron from which the data was collected. In pyramidal neurons, we obtained $M_d^* = 0.724 \pm 0.122$ using the GIF (see fig. 2D3), meaning that the model accurately predicted spiking to within 4 ms $\sim$70 % of the time, after accounting for intrinsic variability in the neural response. It is therefore possible to accurately predict the behaviour of individual L5 mPFC pyramidal neurons with a highly simplified neuron model such as the GIF.

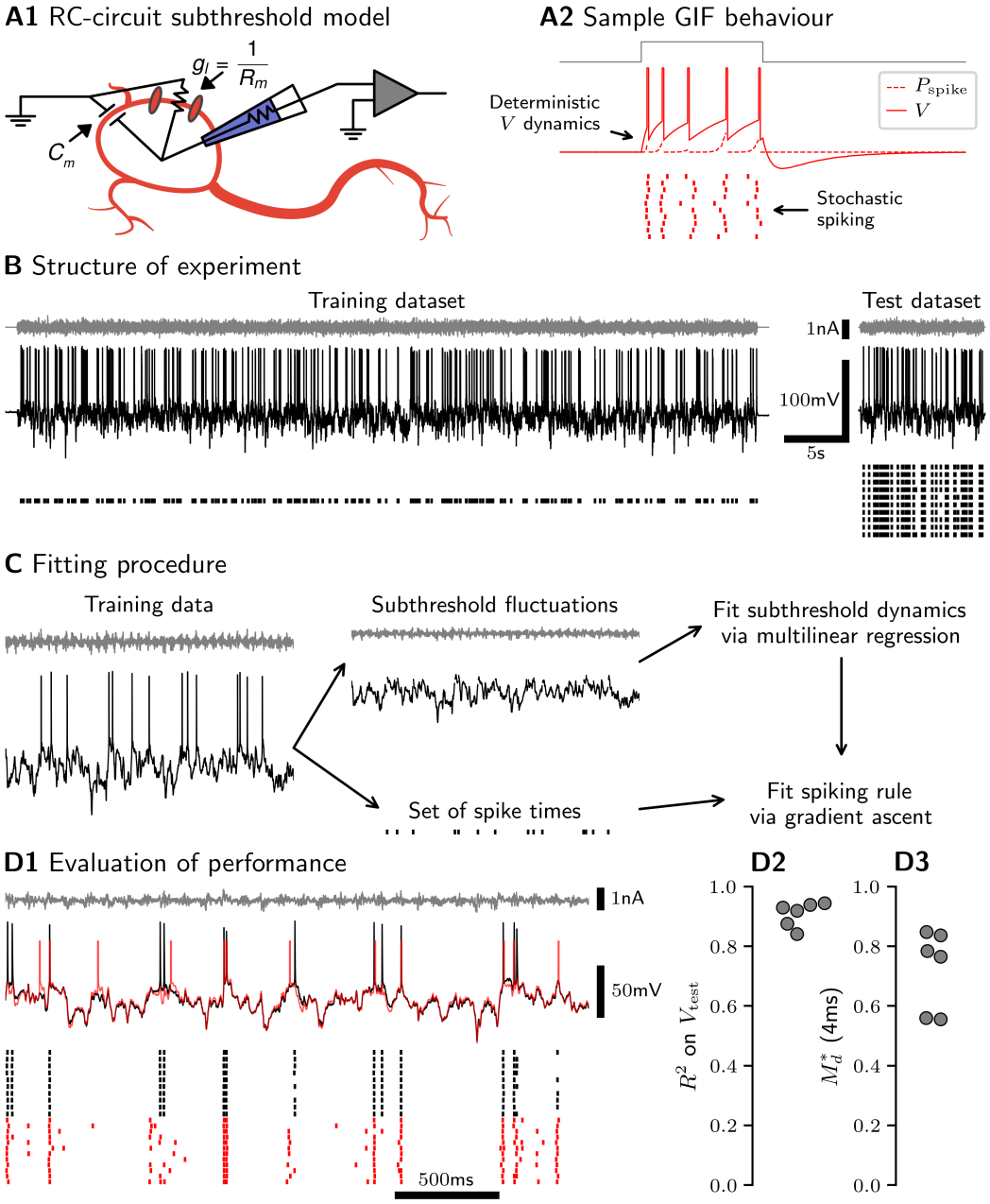

Figure 2: Validation of GIF model using pyramidal neurons. *A.* GIF model sketch. *B.* Structure of a typical experiment. Injected current (top), recorded voltage (middle), and spike raster for all replicates (bottom). Long noisy stimulus used to fit the model (training dataset, left), and multiple repetitions of a shorter stimulus used to evaluate the model (test dataset, right). *C.* Fitting procedure. As previously described [65]. *D.* Evaluation of GIF performance in L5 mPFC neurons. *D1.* Sample test data (black) and model predictions (red). *D2.* Model successfully predicts subthreshold response ($N = 6$ neurons). *D3.* Model successfully predicts spike timing ($N = 6$ neurons). M_d^* quantifies similarity of test set spiketrains and model predictions at a given precision level (4 ms used here). Data collected by Dominic Cyr and Chloe Stewart.

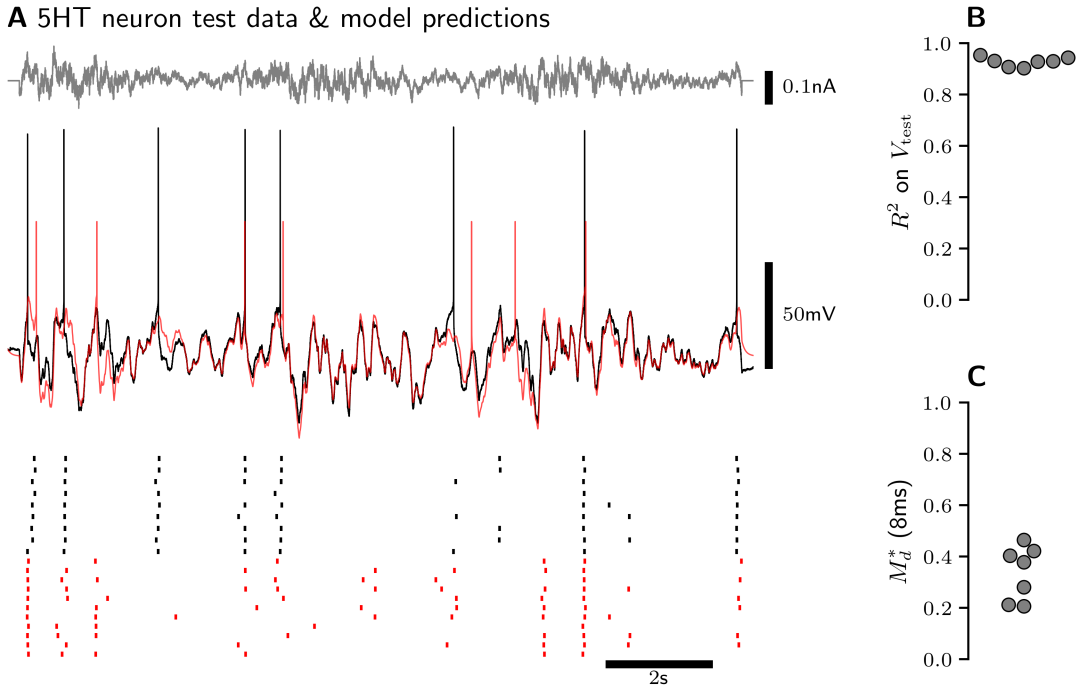

Figure 3: GIF poorly captures 5HT neuron behaviour. *A.* Sample test data (black) and model predictions (red) in a representative 5HT neuron. Noisy current stimulus (top) and voltage response (middle) from a single replicate of test data. Spike raster plot (bottom) for all test data replicates from a single neuron. *B.* Model captures the majority of subthreshold behaviour ($N = 7$ neurons). *C.* Model does not accurately predict spike timing at 8 ms precision ($N = 7$ neurons).

3.3 5HT neurons violate GIF model assumptions

While we found that the GIF was able to predict the firing patterns of mPFC neurons with millisecond precision, it could not readily be tuned to reflect the behaviour of 5HT neurons (see fig. 3A for a representative example). Due to the lower excitability and slower membrane time constant of 5HT neurons compared with pyramidal cells, we collected larger training (60 s $\times$ 3 repetitions) and test (15 s $\times$ 9 repetitions) datasets, used OUN with a longer time constant (50 ms), and lowered the precision used for the M_d^* spiketrain similarity metric (8 ms). Under these conditions, the GIF appeared to accurately capture the subthreshold behaviour of 5HT neurons ($R^2 = 0.927 \pm 0.017$, see fig. 3B), but very poorly predicted their firing patterns ($M_d^* = 0.337 \pm 0.097$, see fig. 3C).

Because the stochastic spiking mechanism employed by the GIF relies on having a good estimate of the subthreshold voltage (see eqn. 3), we hypothesized that the relatively poor performance of the GIF in 5HT neurons with respect to spiking might be rooted in deficiencies of the subthreshold component of the model that are not reflected in the high R^2 value. As a first step towards testing this hypothesis, we asked whether the linear subthreshold model used by the GIF described the subthreshold behaviour of 5HT neurons equally well at rest and near threshold. To control for the contribution of spike-triggered phenomena (i.e., the AHP) to the subthreshold dynamics, we collected a new dataset using slow OUN ($\tau = 200\,\text{ms}$) in the presence of TTX to block spiking. When we fitted the subthreshold model to the resulting data (see fig. 4A), we found that model error depended strongly on voltage (Friedman χ^2 test $p < 0.001$ for $k = 8$ bins from $-80\,\text{mV}$ to $-45\,\text{mV}$ across $N = 14$ cells; see fig. 4B1). In particular, the subthreshold model used by the GIF was significantly less predictive of 5HT neuron behaviour near spike threshold than near resting membrane potential (mean squared error (MSE) at $-60\,\text{mV}$ significantly lower than at $-45\,\text{mV}$, Wilcoxon signed-rank test $p < 0.001$; see fig. 4). In contrast, the same subthreshold model described the behaviour of L5 mPFC pyramidal neurons equally well throughout the subthreshold range (see fig. S1). These observations show that the GIF does not accurately describe the voltage dynamics of 5HT neurons near spike threshold, consistent with the hypothesis that poor performance of the subthreshold component of the GIF in this range may lead to inaccurate spike train predictions. In addition, the fact that the voltage dynamics of 5HT neurons are not well-described by a passive, linear subthreshold model indicates that these cells express voltage-dependent (i.e., nonlinear) conductances that operate in the perithreshold range.

3.4 Characterization of peri-threshold conductances

To understand the contribution of peri-threshold voltage-dependent conductances to the subthreshold dynamics of serotonin neurons, it was first necessary to characterize these conductances in greater detail. Using voltage-clamp experiments, we identified two dissociable

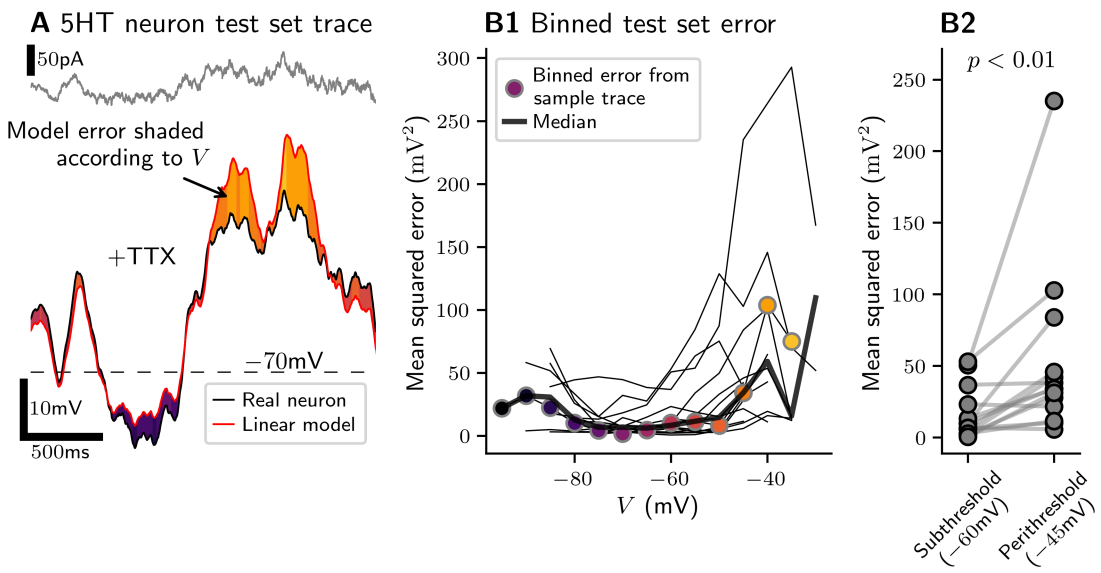

Figure 4: Linear subthreshold model unevenly describes the subthreshold dynamics of 5HT neurons at rest and near threshold. *A*. Sample test data from a 5HT neuron in TTX and corresponding model prediction. Model error is shown in 5 mV bins; areas of the same colour are binned together. *B*. Linear model performance quantified as a function of voltage. *B1*. Model error binned according to the voltage of the real neuron. Fine lines are individual neurons and bold indicates the median. *B2*. Model performs worse near spike threshold ($N = 14$). Gray lines indicate paired data taken from one neuron. p-value is from a Wilcoxon signed-rank test.

conductances that activate in this voltage range: a large outward conductance that inactivated rapidly, and a smaller outward conductance that did not inactivate (see figs. 1D and 5A). Both of these conductances were sensitive to tetraethylammonium (TEA) and 4-aminopyridine (4AP), indicating that both the inactivating and non-inactivating currents are carried by potassium (see fig. 5B). We identified the inactivating current as I_A based on its characteristic voltage-dependence and pharmacology. Multiple voltage- and calcium-activated potassium channels may contribute to the non-inactivating current, which we refer to here as K_{slow}.

Using a voltage-step protocol, we phenomenologically characterized the voltage dependence of these conductances across the voltage range relevant to a spiking neuron model. I_A began to activate near −50 mV, and exhibited a small window current in the −55 mV to −45 mV range (see fig. 5C1). K_{slow} began to activate at more depolarized voltages, near −40 mV (see fig. 5D1). The activation and inactivation curves of both conductances were

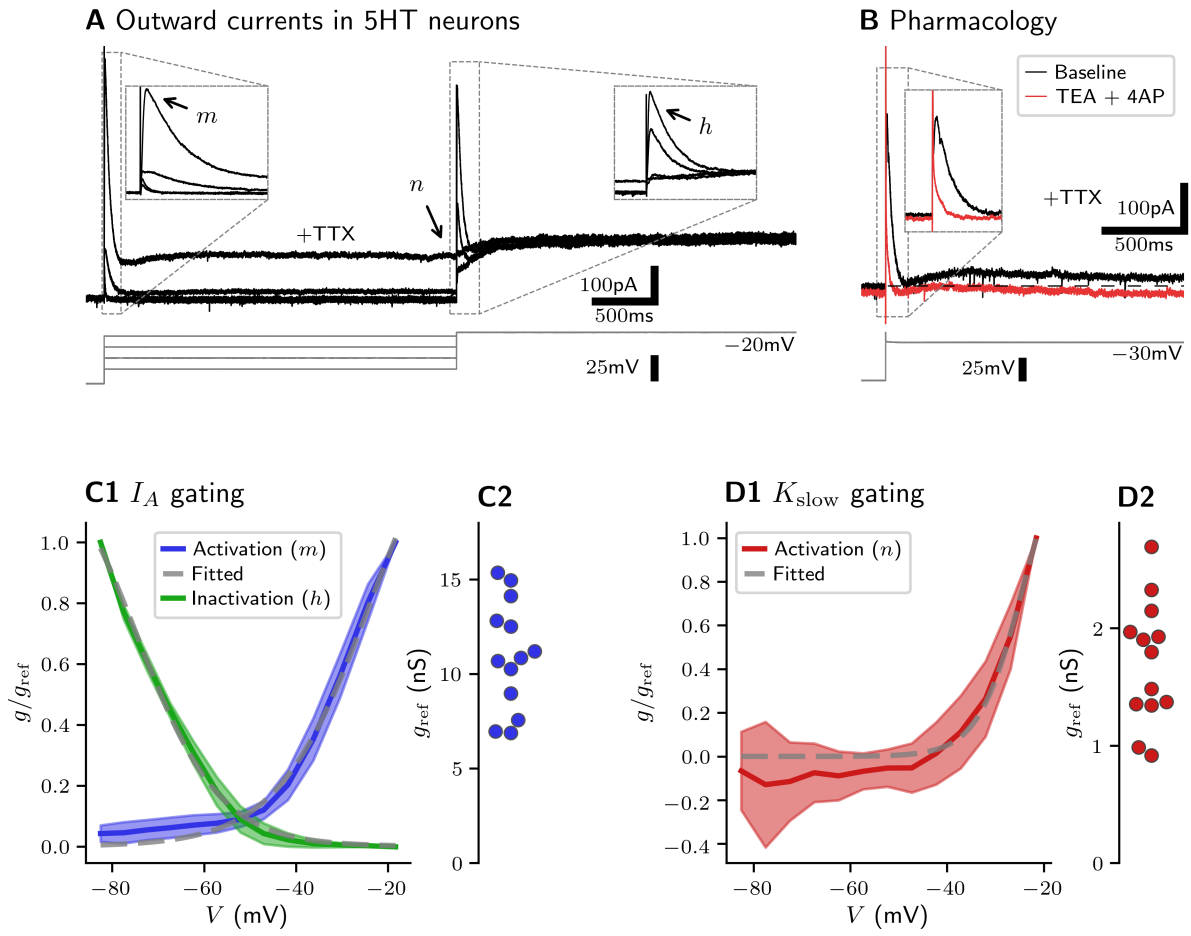

Figure 5: Characterization of perithreshold conductances in 5HT neurons. *A*. Representative leak-subtracted traces showing distinct voltage-dependent outward currents in 5HT neurons. *B*. TEA+4AP-sensitive potassium currents account for almost all of the leak-subtracted outward current. Dashed black line indicates 0 pA. *C1* & *D1*. Voltage dependence of inactivating (mainly I_A) and non-inactivating (termed K_{slow}) potassium currents. Data presented as mean±SD ($N = 13$). Dashed gray lines are sigmoid curves ($g/g_{\text{ref}} = A/(1 + e^{-k(V-V_0)})$) fitted to the data. *C2* & *D2*. Magnitude of inactivating and non-inactivating potassium conductances at −20 mV across cells ($N = 13$; each dot is one neuron).

well-fitted by Boltzmann functions over this restricted voltage range (see fig. 5C1 & D1) with parameter values given in table 1.

To compare the magnitudes of these conductances across cells, we adopted the steady-state activation of each conductance at −20 mV as a reference, pseudo-maximal value. Using this measure, we found that the magnitudes of both I_A (11.00 ± 2.77 nS) and K_{slow} (1.71 ± 0.50 nS) were normally distributed (Shapiro W-test $p = 0.521$ for I_A and $p = 0.857$ for K_{slow}; $N = 13$) and not significantly correlated with eachother (Pearson $R = 0.227$, $p = 0.456$; $N = 13$) (see figs. 5C2 & D2 and fig. S2A). Similar results were obtained using conductance at −40 mV as a reference value (see fig. S2B). These results suggest that DRN 5HT neurons are functionally homogenous with respect to I_A and K_{slow}.

3.5 K_{slow} shapes the subthreshold dynamics of 5HT neurons

To test the contributions of these conductances to the subthreshold dynamics of 5HT neurons, we added them one at a time to our RC-circuit subthreshold model (see eqn. 1) to create a series of augmented leaky integrator models (see eqns. 10–12). When we added I_A alone to the linear RC-circuit model (see eqn. 10), we were surprised to observe that the augmented model did not perform significantly better than the model with the leak conductance alone (see fig. 6A). However, augmenting the linear model with K_{slow} (see eqn. 11) yielded a model that reflects 5HT neuron behaviour throughout the subthreshold range (augmented model error does not depend on voltage, Friedman χ^2 test $p = 0.628$ for $k = 8$ bins from −80 mV to −45 mV across $N = 14$ cells) by selectively improving performance

Table 1: Fitted I_A and K_{slow} gating functions. Parameters are for the Boltzmann function $x_\infty(V) = \frac{A}{1+e^{-k(V-V_{1/2})}}$ fitted to data shown in fig. 5C1 & D1.

Current	**Gate**	**Symbol**	**Boltzmann fit parameters**		
			A	k (**mV**$^{-1}$)	$V_{1/2}$ (**mV**)
I_A	Activation	m_∞	1.61	0.0985	−23.7
	Inactivation	h_∞	1.39	−0.110	−74.7
K_{slow}	Activation	n_∞	1.55	0.216	−24.3

near threshold (K_{slow} model error not different from base model error at $-60\,\text{mV}$, Wilcoxon signed-rank test $p = 0.826$; K_{slow} model error significantly lower than base model error at $-45\,\text{mV}$, Wilcoxon signed-rank test $p < 0.01$; see fig. 6B). When both I_A and K_{slow} were added to the model together (see eqn. 12), we observed a small but statistically-significant improvement in performance compared with the K_{slow} augmented model (combined model error significantly lower than K_{slow}-only model error at both $-60\,\text{mV}$ and $-45\,\text{mV}$, Wilcoxon signed-rank test $p < 0.05$ in each case; see fig. 6C). Taken together, these results show that the peri-threshold nonlinearities in 5HT neuron subthreshold dynamics apparent in our data (see fig. 4) are well-explained by the effect of K_{slow}.

3.6 Effect of I_A on spike timing

Since I_A is abundant in 5HT cells but apparently contributes very little to their subthreshold dynamics, we asked whether this current might have a more potent effect on spike timing. To address this possibility, we constructed a simplified LIF model augmented with I_A and a small amount of subthreshold noise (see eqn. 9). We found that in response to a square input pulse, model neurons with abundant I_A ($\sim 10\times$ leak, comparable to an average 5HT neuron; see fig. 5C2) exhibited increased latency to the first spike and increased spike jitter relative to neurons with little I_A (equal amount of I_A and leak, below the normal range for 5HT cells) (see fig. 7).

Based on our simulations using the augmented LIF model, we hypothesized that I_A robustly modulates spike timing in 5HT neurons. Due to the voltage-dependent inactivation of I_A (see fig. 5D1), it should be possible to distinguish the effect of I_A from other factors that regulate spiking (e.g., cell to cell differences in the leak conductance, stimulus strength, etc.) by its voltage dependence. As shown in fig. 8A1-2, we predict that when neurons with I_A (I_A+) are held near threshold, their response to a square pulse of input should be very similar to that of a neuron without I_A (I_A–). However, when I_A+ neurons are held further from threshold, they can be distinguished from I_A– neurons by the presence

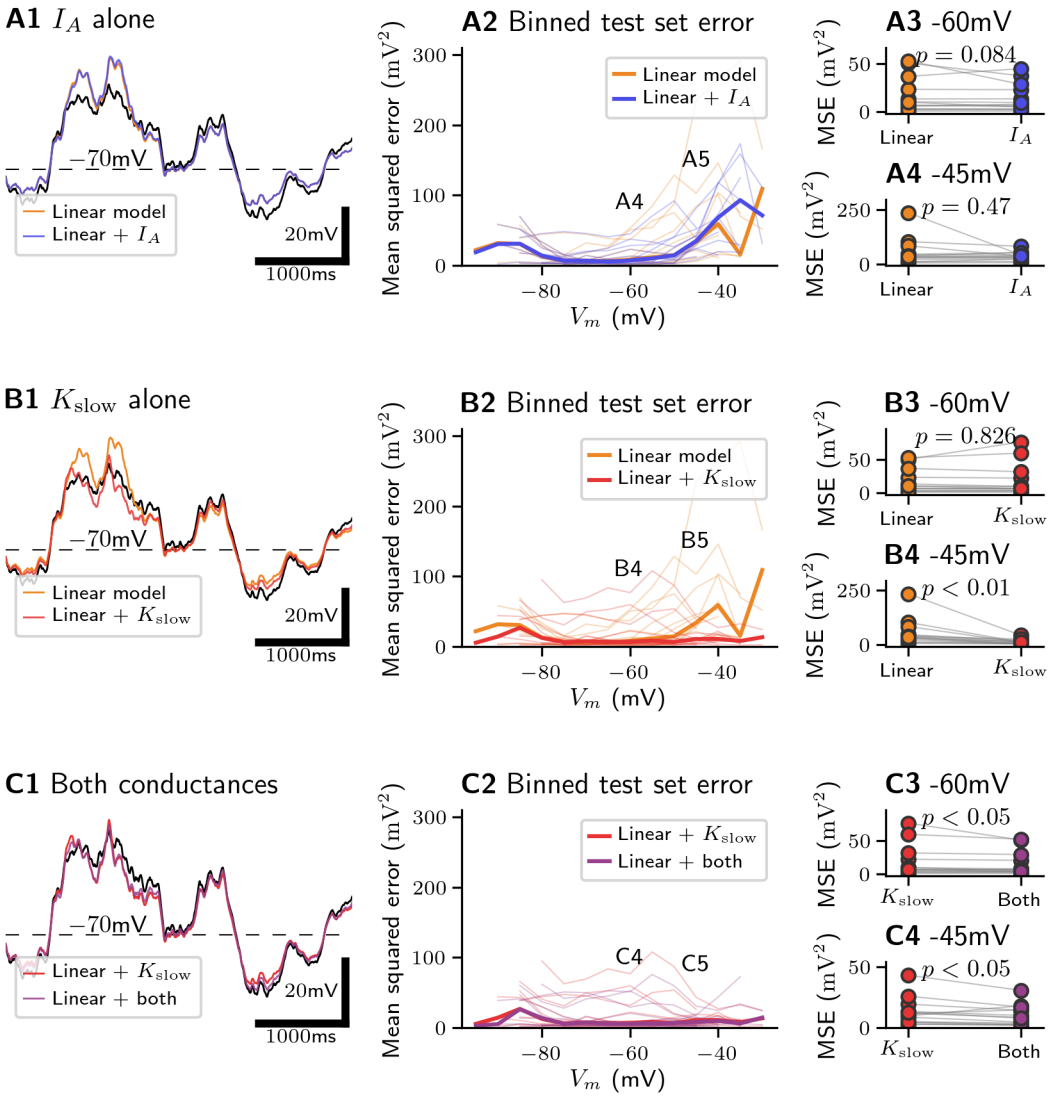

Figure 6: Subthreshold performance of augmented leaky integrator models. *A-C 1.* Sample traces showing neuronal response to a noisy test stimulus (black) and corresponding model predictions. *A-C 2.* Model error binned according to voltage. *A-C 3-4.* Comparison of model error near rest (*A-C 3*) and near threshold (*A-C 4*). Gray lines indicate comparisons within one neuron. p-values are from Wilcoxon signed-rank tests.

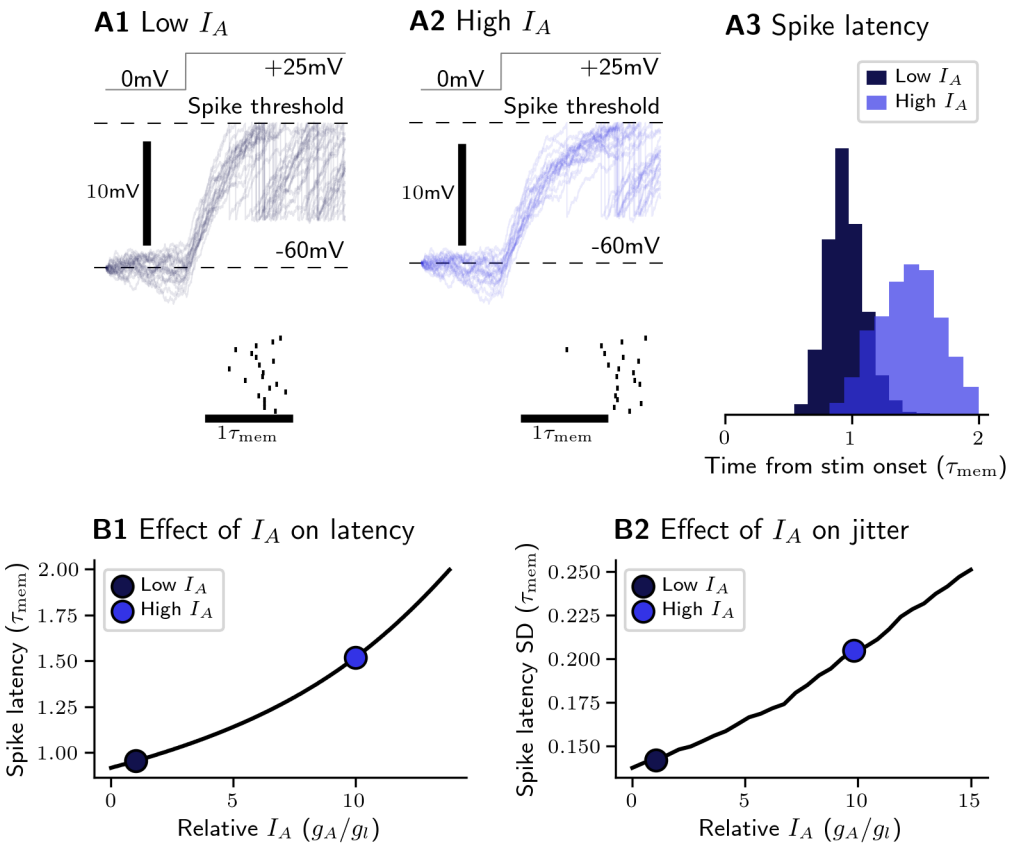

Figure 7: Effect of I_A on spike timing in a simplified model neuron. Model subthreshold dynamics are given by eqn. 9, using $\sigma_{\text{noise}} = 0\,\text{mV}$ in panel *B1* and $\sigma_{\text{noise}} = 2\,\text{mV}$ otherwise. *A*. Comparison of neurons with little I_A (equal amount of I_A and leak) and abundant I_A ($\sim 10\times$ leak). *B*. Specific effects of I_A on spike latency (*B1*) and spike jitter (*B2*).

of a pre-spike shoulder which dramatically increases spike latency. Over a wide range of pre-stimulus potentials, this voltage-dependent shoulder produces a characteristic reverse 'S'-shaped curve in the voltage/spike latency relationship shown in fig. 8A3. In fig. 8B, we see that the behaviour of 5HT neurons fulfills both of these predictions. In response to a square stimulus, 5HT neurons exhibit a pre-spike shoulder that is blocked by 4AP (see fig. 8B1-2), and the voltage/latency relationship displays a reverse 'S'-shaped curve that is well-fitted by the I_A-augmented linear model (see fig. 8B3). Taken together, these observations are persuasive evidence that I_A exerts potent, voltage-dependent control over spike timing in 5HT neurons.

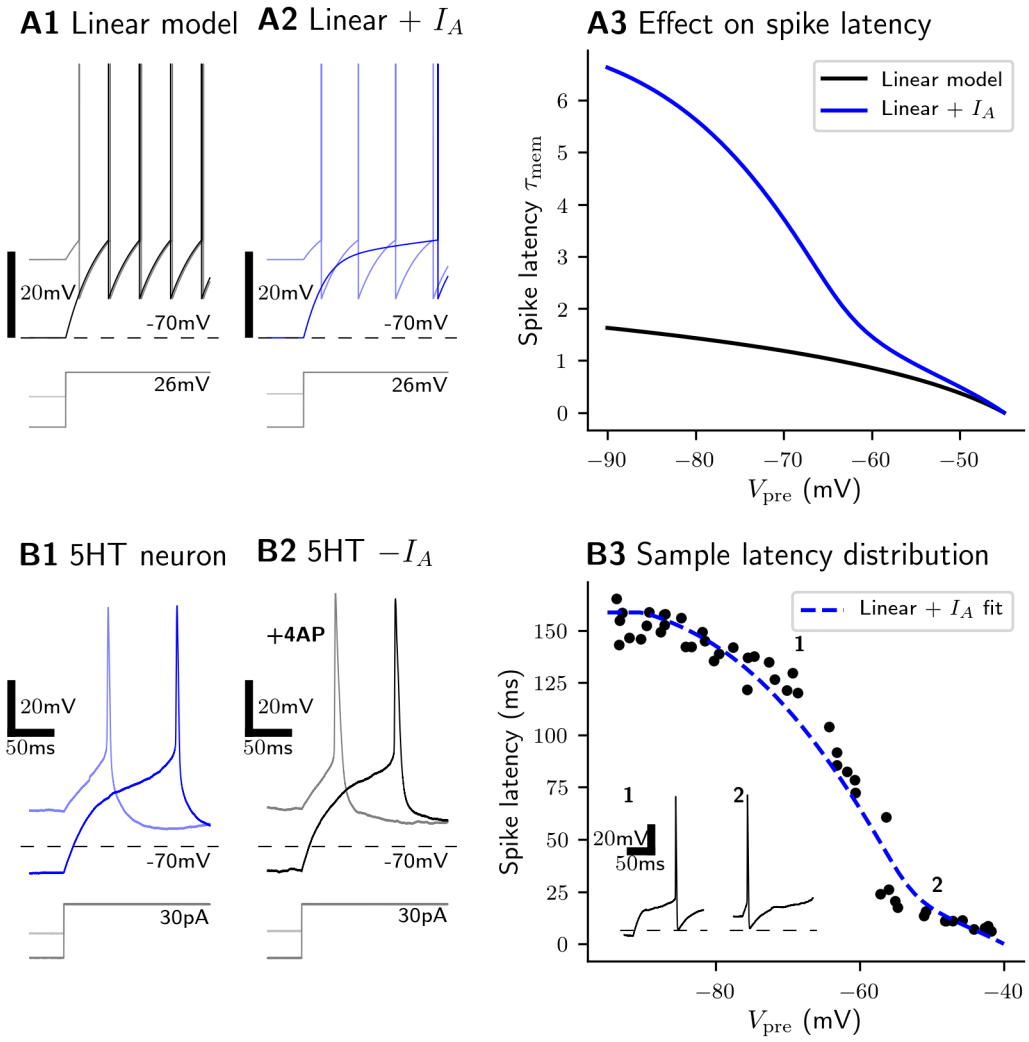

Figure 8: Effect of I_A on spike timing in 5HT neurons. *A*. Voltage-dependent effect of I_A on spike timing in a simplified model neuron. Model subthreshold dynamics are given by eqn. 9, using $\sigma_{\mathrm{noise}} = 0\,\mathrm{mV}$. *A1* and *A2*. Comparison of the responses of neurons with and without I_A to a square stimulus. Note that both neurons respond similarly when already near threshold (pale traces), while only the neuron with $I_A$exhibits a pronounced shoulder in the voltage trace when beginning from a more hyperpolarized potential (darker traces). *A3*. Voltage-dependent effect of I_A on spike latency. Note that spike latency follows a logarithmic curve in the neuron without I_A (black), while the neuron with I_A (blue) shows a pronounced bend near -60mV. *B*. Voltage-dependent effect of I_A on spike timing in 5HT neurons. *B1*. 5HT neuron under control conditions showing voltage-dependent shoulder. *B2*. 5HT neuron under I_A block using 4AP with no shoulder. *B3*. Spike latency distribution as a function of voltage in a different 5HT neuron. Note bend near -60mV and voltage-dependent shoulder in inset.

3.7 Improved performance of KGIF

Based on our findings that K_{slow} and I_A are important regulators of the peri-threshold voltage and firing dynamics of 5HT neurons, respectively, we hypothesized that an augmented GIF model that incorporates these phenomena would better capture the firing behaviour of these cells. To test this hypothesis directly, we combined the augmented subthreshold model containing both conductances (see eqn. 12) with the spiking rules of the GIF to construct a new K-augmented generalized integrate-and-fire (KGIF) model and compared its performance to that of the GIF. As expected, the KGIF did not capture much more of the subthreshold dynamics as measured by R^2 ($R^2 = 0.927 \pm 0.017$ for the GIF and $R^2 = 0.931 \pm 0.034$ for the KGIF, Wilcoxon signed-rank test $p = 0.237$; see fig. 9B), but did significantly improve spiketrain prediction ($M_d^* = 0.310 \pm 0.091$ for the GIF and $M_d^* = 0.477 \pm 0.152$ for the KGIF, Wilcoxon signed-rank test $p < 0.05$; see fig. 9C). It is interesting to note that while the passive membrane properties of 5HT neurons estimated by the GIF and KGIF were similar, as was the estimated spike threshold, the KGIF consistently fitted a *sharper* threshold (i.e., lower ΔV; see eqn. 3) (see fig. S3A). The more deterministic spiking associated with a sharper threshold suggests that the KGIF better estimates the subthreshold behaviours that lead to spiking. Together, these results show that the firing dynamics of DRN 5HT neurons are best described by a model that accounts for the effects of I_A and K_{slow}.

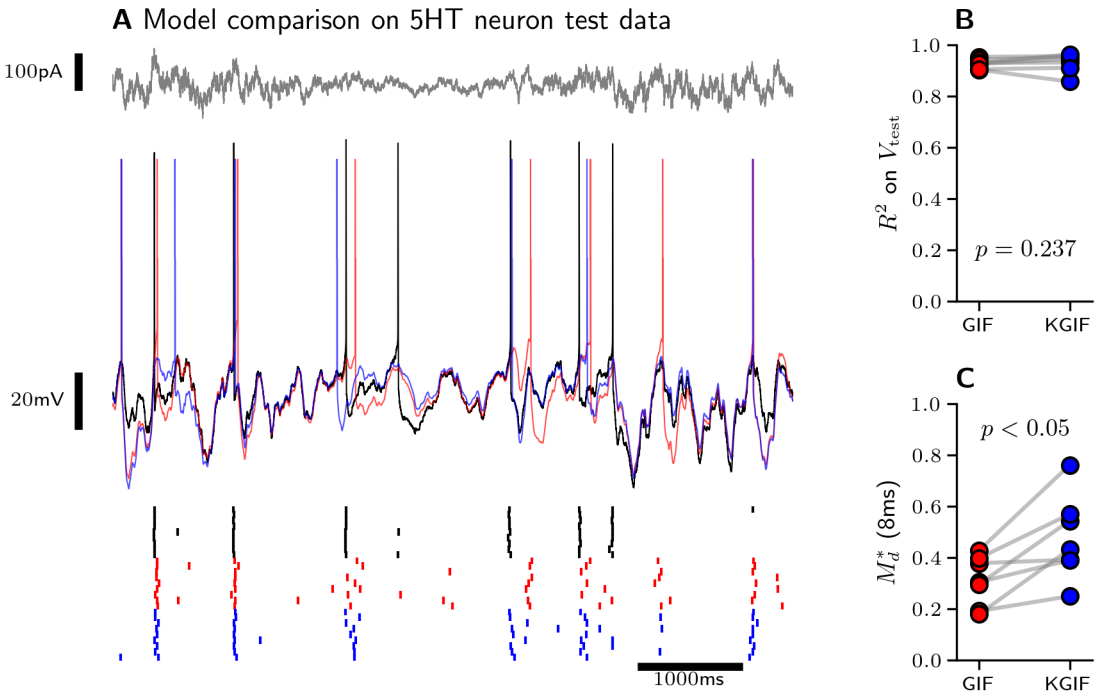

Figure 9: KGIF better explains 5HT neuron behaviour. *A*. Sample test data (black) and model predictions from the GIF (red) and KGIF (blue) in a representative 5HT neuron. Noisy current stimulus (top) and voltage response (middle) from a single replicate of test data. Spike raster plot (bottom) for all test data replicates from a single neuron. *B*. Both models capture the majority of subthreshold behaviour ($N = 6 - 7$ neurons). *C*. KGIF better predicts spike timing at 8 ms precision ($N = 6 - 7$ neurons). p-values are from Wilcoxon signed-rank tests.

4 Discussion

4.1 Apparent homogeneity of 5HT neurons

Several studies have now suggested that 5HT neurons are more electrophysiologically heterogenous than classically believed [25, 34, 69], but does this heterogeneity imply the existence of multiple 5HT neuron types? Our results suggest that 5HT cells with disparate electrophysiological parameters are in fact drawn from the same highly variable population, rather than separate populations with more stereotyped characteristics. Specifically, when we examined the distributions of the minimal set of electrophysiological parameters required to describe the subthreshold dynamics of 5HT neurons, we found that only the membrane time constant was not normally distributed. This was, however, expected, because the membrane time constant $\tau_{mem} = \frac{C}{g_l}$, where C and g_l are both drawn from Gaussian distributions, and the division of two Gaussian distributions produces a gamma distribution that accurately describes our data (not shown). Therefore, based on the distributions of passive membrane properties and the magnitude of I_A and K_{slow}, we cannot reject the hypothesis that 5HT neurons belong to one biophysically-defined population.

In contrast, previous studies in this area have interpreted heterogeneity across biophysical measures to mean that 5HT neurons should not be treated as though they belong to a single population [25, 34, 69]. These divergent conclusions are likely to be due to important methodological differences between this and previous work. First and foremost, two of the three investigations cited have demonstrated differences in the electrophysiological characteristics of 5HT neurons strictly across DRN subregions [25, 69]. Because any comparison of the integrative features of 5HT neurons across subregions is outside the scope of the current work, most of our data was collected from a single subregion (the ventromedial dorsal raphe nucleus (vmDRN)) and the reported differences are therefore unlikely to be apparent in our sample. Using an unsupervised clustering algorithm, one other study has given evidence for

three distinct biophysically-defined 5HT neuron types within the vmDRN [34]. However, because the authors do not report the underlying distributions of the parameters used for clustering, and because the number of clusters detected in a dataset is usually at least partly subjective, it is difficult to know whether the 5HT neuron types identified using this method represent truly separate populations or merely segments of the same underlying population. Finally, all three previous studies distinguish groups of 5HT neurons partly based on electrophysiological parameters that are not likely to be functionally meaningful, such as action potential shape [25, 34, 69]. While differences in the action potential waveform may reflect real differences in the kinetic properties of the voltage-gated channels that mediate action potentials, an important assumption of the LIF-type models used here is that these differences do not affect subthreshold dynamics or spike timing. Because of these methodological differences, our conclusion that 5HT neurons are part of a single, highly variable population is not incompatible with previous work. Instead, our findings represent a refinement of previous results by explicitly parameterizing the biophysical heterogeneity among DRN 5HT neurons.

Recent work has established that multiple qualitatively different spiking phenotypes can arise from a single biophysically-defined population [70]. This is because interactions between the non-linear processes that regulate excitability (e.g. the voltage-dependence of spike probability, or the dynamics of voltage-gated ion channels) can produce large, qualitative shifts in firing dynamics in response to only small changes in the parameters of the underlying processes [70, 71]. When these qualitative shifts arise in response to infinitesmally small changes in the underlying biophysical parameters, they are referred to as bifurcations. Recent work has demonstrated that depending on the amount of I_A and the amplitude of injected current, the firing dynamics of different cells from the same population (or even within an individual neuron) can lie on either side of a bifurcation [70]. For example, under conditions of abundant I_A and a weak step current stimulus, neurons fire trains of action potentials with a large latency to the first spike. However, if the magnitude of I_A is decreased or the

amplitude of the current increased slightly, it is possible to emit a spike with a very short latency [70]. In our data, this effect is loosely reflected by the much shorter spike latency when I_A is inactivated using voltage (see fig. 8B3). Because we have shown that I_A plays a key role in shaping the firing dynamics of 5HT neurons, but that the magnitude of this conductance varies substantially from cell to cell, it is possible that some subpopulations of DRN 5HT neurons exhibit qualitatively different responses to identical stimuli. Conversely, because the same spiking phenotype can arise from multiple combinations of ion channel densities [72], it is possible that the firing patterns of 5HT neurons are in instead *more* homogenous than the observed variability in the expression of I_A and K_{slow} would suggest. This work provides a simplified neuron model capable of capturing the effects of both of these conductances on cell excitability, along with empirically-constrained parameter estimates for DRN 5HT neurons. In the future, a detailed analysis of our model could shed light on the nature of the relationship between biophysical and functional heterogeneity in the DRN.

4.2 Electrophysiological characteristics of peri-threshold conductances

4.2.1 Properties of K_{slow}

Voltage-dependent potassium currents play an important role in regulating the firing behaviour and subthreshold dynamics of 5HT neurons. The whole-cell outward current mediated by voltage-gated potassium channels exhibits a fast component, which activates within milliseconds and inactivates over tens of milliseconds, and a slow component, which does not inactivate appreciably in our experiments (see fig. 5A & B). While we have identified the fast component as I_A based on its activation at subthreshold voltages and sensitivity to 4AP, we have not positively identified the source of the non-inactivating component, referred to as K_{slow}.

Several potassium currents that have been reported in DRN neurons may contribute

to K_{slow}. These include M-type potassium current, which activates below threshold and inactivates over seconds; delayed rectifier potassium current, which activates near $-40\,\text{mV}$ and does not inactivate; and big- or small-conductance calcium-activated potassium channels (reviewed in [58]). These currents are highly similar from a functional perspective in that their activation and/or inactivation dynamics evolve over either significantly slower or faster timescales than the intrinsic membrane dynamics of 5HT neurons ($\sim$60 ms time constant). Their time dynamics can therefore safely be ignored without drastically altering the dynamics of a simplified neuron model. Because the time dynamics of the underlying current(s) are unlikely to be critical and our model accurately reproduces the voltage-dependence of the outward current observed in these cells, our phenomenological K_{slow} current provides an adequate description of a key process that regulates the subthreshold dynamics of 5HT neurons.

4.2.2 Properties of I_A

First discovered in the neurons of the marine gastropod *Anisodoris* [73], I_A is an inactivating voltage-dependent potassium current with biophysical properties that vary between cell types. Although I_A begins to activate below spike threshold, at steady state it is normally almost completely inactivated at resting membrane potential [74]. In general, I_A activates very quickly in response to depolarizing voltage steps (τ<5 ms) and inactivates monoexponentially over tens of milliseconds [74]. In mammalian neurons, I_A is mediated by multiple potassium channel types from the Shal family: $K_v4.1$, $K_v4.2$, and $K_v4.3$. The properties of Shal potassium channels are determined mainly by their large, pore-forming α subunits, which differ in their expression patterns in mammalian brain [75] as well as their voltage-dependence and kinetics [76]. Because the properties of I_A can vary between cell types, we chose to characterize it in 5HT neurons.

I_A has been reported in DRN neurons a handful of times in the literature [77–79], but, to our knowledge, the present work is the first characterization of I_A in genetically-identified

5HT cells. In our hands, the activation and inactivation curves of I_A in 5HT cells were well-described by a pair of first-order Boltzmann functions with parameters very close to the mean values reported for other cell types, except for a smaller slope value of inactivation curve in 5HT neurons (see table 2). Compared with previous characterizations of I_A in DRN neurons, we found that I_A inactivated at more depolarized voltages (possibly reflecting species or cell-type differences), but our results are otherwise similar. Because we show here that the voltage-dependence of I_A is homogenous and well-described by a pair of first-order Boltzmann functions across a relatively large sample of genetically-identified 5HT neurons ($N = 13$), our work sheds light on the previously not well characterized properties of I_A in these cells.

The voltage-dependence of I_A in 5HT cells helps explain the potent effects of this current on spike timing observed in our data. Whereas in other cell types I_A is mostly inactivated at rest [74], in 5HT neurons $V_{1/2}$ of the inactivation curve is very close to the resting membrane potential ($V_{1/2}$ =−74.7 mV, mean V_{rest} =−68.7 mV). Because the midpoint of the inactivation function aligns with the resting membrane potential of 5HT cells and the slope of the inactivation curve is shallow compared with other cell types, I_A in 5HT neurons is likely to be subject to relatively little inactivation in the subthreshold regime. These characteristics enable I_A to play a particularly important part in shaping the behaviour of 5HT neurons.

4.3 Functional effects of I_A

4.3.1 Regulation of firing dynamics by I_A

In this work, we have presented evidence that I_A is an important regulator of firing dynamics in 5HT neurons. Using complementary experimental and computational approaches, we have shown that I_A acts as a voltage-dependent regulator of spike latency in response to strong inputs (see figs. 7 & 8). Using a simplified LIF neuron with I_A, we have further predicted that I_A in 5HT neurons also jitters spike timing (see fig. 7B2). These findings support and

Table 2: Comparison of I_A voltage-dependence with literature values. All parameters are for first-order Boltzmann functions $x_\infty(V) = \frac{A}{1+e^{-k(V-V_{1/2})}}$.

Cell type	**Reference**	**Activation function parameters**		**Inactivation function parameters**	
		k (mV^{-1})	$V_{1/2}$ (mV)	k (mV^{-1})	$V_{1/2}$ (mV)
Positively-identified 5HT neurons	Here	0.0985	-23.7	-0.110	-74.7
DRN neurons	[79]	0.0606	-25.0	-0.108	-91.5
	[77] (analyzed in [58])	0.125	NA	-0.167	-78.0
Various (10 cell types, 15 publications)	[74]	0.0851 ± 0.0479	-22.6 ± 14.7	-0.139 ± 0.021	-74.0 ± 9.4

extend a rich body of literature on the involvement of I_A in regulating spike timing.

I_A has been reported to exert voltage-dependent control over spike timing in a wide range of cell types and model organisms [70, 80–86]. Particular attention has been paid to the effect of I_A on spike latency in response to a strong stimulus preceded by a period of quiescence, first observed in the central pattern generating swim interneurons of *Tritonia diomedea*, a marine gastropod mollusk [80]. Voltage-dependent inhibition is a canonical feature of I_A, and it is interesting to note that the hyperpolarization necessary to de-inactivate I_A can be provided by inhibitory synaptic input [81] as well as from a lack of excitatory drive. In the former case, the voltage dependence of I_A leads to complex, nonlinear interactions between synaptic sources of inhibition and I_A, which is thought to implement a type of contrast-enhancement in sensory systems [81]. Whatever the mechanism of de-inactivation, several groups have now demonstrated that I_A delays the onset of firing by tens of milliseconds (depending on stimulus strength and pre-pulse voltage) in neurons of mammalian [84, 86] and non-mammalian [81, 82] vertebrates. The magnitude of this effect is roughly consistent with our own findings. Based on the change in latency when I_A is inactivated using voltage, I_A can modulate spike timing by approximately 10 ms to 100 ms in 5HT neurons under our conditions (see fig. 8B3); similar to what has been observed previously in unidentified DRN cells [78]. The fact that this range shows substantial overlap with the distribution of membrane time constants found in 5HT neurons (approximately 40 ms to 100 ms, see fig. 1F3) illustrates that the functional effect of I_A occupies a similar timescale to the passive membrane dynamics of 5HT neurons. This suggests that the dynamics of I_A cannot be ignored due to separation of timescales when the general integrative features of 5HT neurons are being considered. Because this current is known to influence the spiking behaviour of other cell types, including some thalamic relay cells [86] and pyramidal neurons of the electrosensory lateral line lobe of weakly electric fish [82, 85], our model of the impact of I_A on spike latency and jitter may shed light on the functional properties of other neuronal populations.

The effect of inactivating potassium currents on spike jitter has received little attention

in the literature. One study has demonstrated that I_D (an inactivating potassium current similar to I_A in terms of voltage-dependence and pharmacology, but with slower inactivation kinetics) increases spike jitter in CA1 pyramidal cells [87]. In it, the authors show that blocking I_D (but not I_A, which is not active below threshold in CA1 neurons) using dendrotoxin, low concentrations of 4AP, or voltage inactivation decreases the coefficient of variation of spikes elicited by a square stimulus. Since I_A and I_D are both sensitive to the high concentrations of 4AP used here, and mRNA for $K_v1.2$ (a member of the Shaker family of ion channels that mediate I_D) is expressed in some DRN cells [88], it is possible that I_D contributes to our phenomenological I_A current. Because I_A and I_D are functionally similar, these observations support our prediction that I_A increases spike jitter in 5HT cells. These convergent findings suggest that the jittering effect of transient hyperpolarizing currents may be a general principle of neural integration.

4.3.2 Potential impact of I_A on ensemble learning in the DRN

So far we have discussed the functional properties of DRN 5HT neurons as though they are part of a static network, but previous work carried out by our group shows that this is not the case [29, 54]. It is therefore important to consider whether the impact of the potassium conductances we describe on the intrinsic excitability of 5HT neurons could precipitate changes in the structure of the DRN network. Here we discuss one possible mechanism through which this could occur: that I_A might modulate the expression of spike time dependent plasticity (STDP).

STDP is a plasticity rule according to which presynaptic activity that is closely followed by a post-synaptic action potential leads to potentiation of the recently-activated synapses, whereas the opposite sequence leads to synaptic depression [89]. In 5HT neurons STDP has received little attention, but one recent publication has demonstrated that long-term potentiation (LTP) can be observed with a 5 ms interval between pre- and post-synaptic activity in this population [90]. Although the precise time-dependence of this effect is not known, it is

interesting to consider whether I_A could inhibit this LTP by prolonging the interval between presynaptic activity and post-synaptic spiking under physiological conditions. If this is the case, suppression of I_A, for instance by noradrenergic input [77], might provide a mechanism to modulate this phenomenon, effectively tuning the rate of synaptic potentiation in the DRN.

4.4 Limitations of the GIF and KGIF

Although the KGIF better captures the behaviour of DRN 5HT neurons than the GIF, it does not predict the firing patterns of these cells as precisely as the GIF does those of cortical neurons. According to the M_d^* spiketrain similarity metric, the GIF predicted L5 pyramidal neuron spikes to within 4 ms $\sim$70 % of the time after correcting for intrinsic variability in the neural response (compared with $\sim$75 % previously reported in somatosensory cortex L5 pyramidal neurons [65]), whereas even the KGIF only predicted 5HT neuron spikes to within 8 ms $\sim$50 % of the time. This difference in performance is likely due to a combination of experimental factors that limit model performance as well as physiological processes that are not captured by the GIF and KGIF.

Non-physiological factors that may affect model performance include the finite amount of data available to fit each model and the choice of fitting algorithm. In particular, the low intrinsic excitability and slow time constant of 5HT neurons limit the amount of data available to effectively constrain the GIF and KGIF models. In spite of collecting three times more data per neuron from 5HT cells than from pyramidal neurons, much fewer spikes were available in the 5HT neuron recordings to constrain the models. As a result, the GIF and KGIF models fitted to 5HT neurons may have become more biased, reducing test set performance. Arguing against this idea is the fact that the GIF achieves near-optimal performance in pyramidal neurons when fitted to data containing only $\sim$ 100 spikes [65], close to the 122.7 ± 68.6 (range 61 to 283) spikes/cell in our data. The lower performance on spike prediction in 5HT cells is therefore not likely to be due to sampling bias caused by

the smaller number of spikes in the 5HT neuron data.

Another potential source of model bias that could limit the accuracy of spike train predictions is the design of the algorithm used to fit the models to the training data. This is particularly important in the case of the procedure used to extract the maximal conductances of I_A and K_{slow} ($\bar{g}_A$ and $\bar{g}_{\text{slow}}$, respectively) for the KGIF. We used ordinary least-squares (OLS) multilinear regression to fit these coefficients based on the subthreshold traces, but it is possible that this approach does not produce optimal spiketrain predictions. This is because the values of $\bar{g}_A$ and $\bar{g}_{\text{slow}}$ obtained by OLS are estimated based on equal weighting of all points in the subthreshold trace. In our traces, most of the datapoints are concentrated around the mean subthreshold potential of $\sim$−60 mV where I_A and K_{slow} are minimally activated, with relatively few points $>$−45 mV where both conductances play a potent role in shaping the subthreshold dynamics. Our estimates of $\bar{g}_A$ and $\bar{g}_{\text{slow}}$ obtained by OLS regression may therefore not optimally describe the behaviour of 5HT neurons in the peri-threshold voltage range over which I_A and K_{slow} are most active. Use of an alternative approach such as weighted least-squares may lead to $\bar{g}_A$ and $\bar{g}_{\text{slow}}$ estimates that are more similar to their measured values and improved spike train predictions.

The lower performance of the GIF and KGIF in 5HT neurons also raises important questions about whether there are physiological processes that regulate spike initiation in 5HT neurons that are not included in our model. One possibility is that there are additional subthreshold conductances that participate in shaping the firing dynamics of these cells. T-type calcium conductance is an important contender for this role because it is active at subthreshold potentials, regulates firing patterns in other cell types [91], and is present in some DRN neurons [92]. This low-voltage calcium conductance could regulate spike timing both through direct depolarization and by delayed activation of calcium-dependent potassium currents. While a previous detailed conductance-based 5HT neuron model included a T-type current [58], we have not included it in our phenomenological model because the characteristic transient inward current mediated by T-type calcium channels was not apparent

in our data.

Another potential explanation for the lower predictive power of our model is that TTX-sensitive sodium current participates in regulating spike *timing* in addition to action potential shape. Like other integrate-and-fire models, our GIF and KGIF assume that this is not the case. Recent data show that the progressive inactivation of sodium channels during repetitive firing in 5HT neurons regulates spike threshold [93]. While both the GIF and KGIF account for spike-triggered changes in action potential threshold, they do not account for partial inactivation of sodium channels at subthreshold voltages during the time leading up to isolated spikes. A variant of the GIF that explicitly accounts for this phenomenon better predicts the spike trains of pyramidal neurons [67]. Because I_A increases spike latency by holding neurons near threshold for extended periods, peri-threshold inactivation of sodium channels may play a particularly important role in regulating spike timing in cells with a high level of I_A. Therefore, a 5HT neuron model that also accounts for voltage-dependent modulation of spike threshold may provide a better description of the firing behaviour of these cells than the minimal model presented here.

Finally, it is possible that the complex effects of cell morphology and compartmentalized expression of ion channels participate in shaping the integrative features of 5HT neurons in ways that cannot be captured by the point neuron models used here. It is unlikely that ionic currents in distal compartments play an important role in filtering the input used to fit the models because the GIF and KGIF are trained on data using somatic current injection. Consistent with this idea, the firing behaviour of cortical pyramidal neurons, which are known to express a menagerie of ion channels segregated across various compartments, is easily captured by the GIF [65]. Therefore, although a morphologically-detailed model might provide a better description of how 5HT neurons integrate synaptic inputs, it would not be likely to provide a significantly better description of the intrinsic excitability of these cells than the simplified model presented here. Furthermore, the complexity of morphologically-detailed models makes them prohibitively difficult to constrain to individual neurons, meaning that

they cannot easily reflect cell-to-cell heterogeneity.

The KGIF accounts for the dominant factors that regulate 5HT neuron excitability present in our experiments, but does not perfectly reflect the spiking behaviour of these cells. Optimizing the fitting procedure and accounting for the effect of sodium channel inactivation on spike threshold are the most promising avenues towards improving the KGIF. However, these and other possible optimizations may produce diminishing returns, and come at the expense of added computational complexity. The KGIF therefore represents a compromise well-suited to applications in network modelling that demand a lightweight single neuron model rather than millisecond precision.

4.5 Conclusion

How the complex network architecture of the DRN supports its nuanced role in regulating behaviour is not well understood. As the first step towards a bottom-up understanding of DRN network dynamics, we present a simplified 5HT neuron model suitable for network-level simulations. Using complementary experimental and computational methods, we have identified two phenomenological potassium currents that play important roles in shaping the subthreshold dynamics and firing behaviour of these cells. In particular, we have shown that an A-type potassium conductance with highly variable density in 5HT neurons regulates spike latency and jitter. Our analysis provides a foundation for future work to determine how these properties shape information processing in the DRN and other similar networks.

References

1. Warden, M. R. *et al.* A prefrontal cortex–brainstem neuronal projection that controls response to behavioural challenge. *Nature* **492,** 428–432 (2012).
2. Young, S. N., Smith, S. E., Pihl, R. O. & Ervin, F. R. Tryptophan depletion causes a rapid lowering of mood in normal males. *Psychopharmacology* **87,** 173–177 (1985).
3. Delgado, P. L. *et al.* Serotonin and the Neurobiology of Depression: Effects of Tryptophan Depletion in Drug-Free Depressed Patients. *Archives of General Psychiatry* **51,** 865 (1994).
4. Cipriani, A. *et al.* Comparative efficacy and acceptability of 21 antidepressant drugs for the acute treatment of adults with major depressive disorder: a systematic review and network meta-analysis. *The Lancet* **391,** 1357–1366 (2018).
5. Schultz, W., Dayan, P. & Montague, P. R. A Neural Substrate of Prediction and Reward. *Science* **275,** 1593–1599 (1997).
6. Dayan, P. & Huys, Q. Serotonin's many meanings elude simple theories. *eLife* **4** (2015).
7. Li, Y. *et al.* Serotonin neurons in the dorsal raphe nucleus encode reward signals. *Nature Communications* **7,** 10503 (2016).
8. Zhong, W., Li, Y., Feng, Q. & Luo, M. Learning and Stress Shape the Reward Response Patterns of Serotonin Neurons. *The Journal of Neuroscience* **37,** 8863–8875 (2017).
9. Luo, M., Li, Y. & Zhong, W. Do dorsal raphe 5-HT neurons encode beneficialness? *Neurobiology of Learning and Memory* **135,** 40–49 (2016).
10. Cohen, J. Y., Amoroso, M. W. & Uchida, N. Serotonergic neurons signal reward and punishment on multiple timescales. *eLife* **4** (2015).
11. Hayashi, K., Nakao, K. & Nakamura, K. Appetitive and Aversive Information Coding in the Primate Dorsal Raphé Nucleus. *The Journal of Neuroscience* **35,** 6195–6208 (2015).
12. Ren, J. *et al.* Anatomically Defined and Functionally Distinct Dorsal Raphe Serotonin Sub-systems. *Cell* (2018).
13. Miyazaki, K. W. *et al.* Optogenetic Activation of Dorsal Raphe Serotonin Neurons Enhances Patience for Future Rewards. *Current Biology* **24,** 2033–2040 (2014).
14. Fonseca, M. S., Murakami, M. & Mainen, Z. F. Activation of Dorsal Raphe Serotonergic Neurons Promotes Waiting but Is Not Reinforcing. *Current Biology* **25,** 306–315 (2015).
15. Miyazaki, K. *et al.* Reward probability and timing uncertainty alter the effect of dorsal raphe serotonin neurons on patience. *Nature Communications* **9,** 2048 (2018).
16. Iigaya, K., Fonseca, M. S., Murakami, M., Mainen, Z. F. & Dayan, P. An effect of serotonergic stimulation on learning rates for rewards apparent after long intertrial intervals. *Nature Communications* **9,** 2477 (2018).
17. Correia, P. A. *et al.* Transient inhibition and long-term facilitation of locomotion by phasic optogenetic activation of serotonin neurons. *eLife* **6** (2017).

18. Liu, Z. *et al.* Dorsal Raphe Neurons Signal Reward through 5-HT and Glutamate. *Neuron* **81,** 1360–1374 (2014).

19. Lottem, E. *et al.* Activation of serotonin neurons promotes active persistence in a probabilistic foraging task. *Nature Communications* **9,** 1000 (2018).

20. Marcinkiewcz, C. A. *et al.* Serotonin engages an anxiety and fear-promoting circuit in the extended amygdala. *Nature* **537,** 97–101 (2016).

21. Vertes, R. P. & Crane, A. M. Distribution, quantification, and morphological characteristics of serotonin-immunoreactive cells of the supralemniscal nucleus (B9) and pontomesencephalic reticular formation in the rat. *The Journal of Comparative Neurology* **378,** 411–424 (1997).

22. Descarries, L., Watkins, K. C., Garcia, S. & Beaudet, A. The serotonin neurons in nucleus raphe dorsalis of adult rat: A light and electron microscope radioautographic study. *The Journal of Comparative Neurology* **207,** 239–254 (1982).

23. Steinbusch, H. Distribution of serotonin-immunoreactivity in the central nervous system of the rat—Cell bodies and terminals. *Neuroscience* **6,** 557–618 (1981).

24. Vertes, R. P. A PHA-L analysis of ascending projections of the dorsal raphe nucleus in the rat. *The Journal of Comparative Neurology* **313,** 643–668 (1991).

25. Calizo, L. H. *et al.* Raphe serotonin neurons are not homogenous: Electrophysiological, morphological and neurochemical evidence. *Neuropharmacology* **61,** 524–543 (2011).

26. Gagnon, D. & Parent, M. Distribution of VGLUT3 in Highly Collateralized Axons from the Rat Dorsal Raphe Nucleus as Revealed by Single-Neuron Reconstructions. *PLoS ONE* **9** (ed Bader, M.) e87709 (2014).

27. Ramamoorthy, S. *et al.* Antidepressant- and cocaine-sensitive human serotonin transporter: molecular cloning, expression, and chromosomal localization. *Proceedings of the National Academy of Sciences* **90,** 2542–2546 (1993).

28. Weissbourd, B. *et al.* Presynaptic Partners of Dorsal Raphe Serotonergic and GABAergic Neurons. *Neuron* **83,** 645–662 (2014).

29. Geddes, S. D. *et al.* Target-specific modulation of the descending prefrontal cortex inputs to the dorsal raphe nucleus by cannabinoids. *Proceedings of the National Academy of Sciences* **113,** 5429–5434 (2016).

30. Wang, R. Y. & Aghajanian, G. K. Correlative firing patterns of serotonergic neurons in rat dorsal raphe nucleus. *Journal of Neuroscience* **2,** 11–16 (1982).

31. Aghajanian, G. & Vandermaelen, C. Intracellular identification of central noradrenergic and serotonergic neurons by a new double labeling procedure. *The Journal of Neuroscience* **2,** 1786–1792 (1982).

32. Aghajanian, G. K. & Vandermaelen, C. P. Intracellular recordings from serotonergic dorsal raphe neurons: pacemaker potentials and the effect of LSD. *Brain Research* **238,** 463–469 (1982).

33. Vandermaelen, C. & Aghajanian, G. Electrophysiological and pharmacological characterization of serotonergic dorsal raphe neurons recorded extracellularly and intracellularly in rat brain slices. *Brain Research* **289,** 109–119 (1983).

34. Fernandez, S. P. *et al.* Multiscale single-cell analysis reveals unique phenotypes of raphe 5-HT neurons projecting to the forebrain. *Brain Structure and Function* **221,** 4007–4025 (2016).

35. Templin, J. S., Bang, S. J., Soiza-Reilly, M., Berde, C. B. & Commons, K. G. Patterned expression of ion channel genes in mouse dorsal raphe nucleus determined with the Allen Mouse Brain Atlas. *Brain Research* **1457,** 1–12 (2012).

36. Fu, W. *et al.* Chemical neuroanatomy of the dorsal raphe nucleus and adjacent structures of the mouse brain. *The Journal of Comparative Neurology* **518,** 3464–3494 (2010).

37. Prouty, E. W., Chandler, D. J. & Waterhouse, B. D. Neurochemical differences between target-specific populations of rat dorsal raphe projection neurons. *Brain Research* **1675,** 28–40 (2017).

38. Priestley, J., Wotherspoon, G., Savery, D., Averill, S. & Rattray, M. A combined in situ hybridization and immunofluorescence procedure allowing visualisation of peptide mRNA and serotonin in single sections. *Journal of Neuroscience Methods* **48,** 99–110 (1993).

39. Léon, M. d. *et al.* Distribution of Somatostatin-28 (I-12) in the Cat Brainstem: an lmmunocytochemical Study. *Neuropeptides* **21,** 1–11 (1992).

40. Fodor, M. *et al.* Distribution and pharmacological characterization of somatostatin receptor binding sites in the sheep brain. *Journal of Chemical Neuroanatomy* **12,** 175–182 (1997).

41. Araneda, S., Gysling, K. & Calas, A. Raphe serotonergic neurons projecting to the olfactory bulb contain galanin or somatostatin but not neurotensin. *Brain Research Bulletin* **49,** 209–214 (1999).

42. Anhaou, A. *et al.* Immunocytochemical Distribution of VIP and PACAP in the Rat Brain Stem: Implications for REM Sleep Physiology. *Annals of the New York Academy of Sciences* **1070,** 135–142 (2006).

43. Petit, J.-M., Luppi, P.-H., Peyron, C., Rampon, C. & Jouvet, M. VIP-like immunoreactive projections from the dorsal raphe and caudal linear raphe nuclei to the bed nucleus of the stria terminalis demonstrated by a double immunohistochemical method in the rat. *Neuroscience Letters* **193,** 77–80 (1995).

44. Gocho, Y., Sakai, A., Yanagawa, Y., Suzuki, H. & Saitow, F. Electrophysiological and pharmacological properties of GABAergic cells in the dorsal raphe nucleus. *The Journal of Physiological Sciences* **63,** 147–154 (2013).

45. Abrams, J. K., Johnson, P. L., Hollis, J. H. & Lowry, C. A. Anatomic and Functional Topography of the Dorsal Raphe Nucleus. *Annals of the New York Academy of Sciences* **1018,** 46–57 (2004).

46. Lowry, C. A., Johnson, P. L., Hay-Schmidt, A., Mikkelsen, J. & Shekhar, A. Modulation of anxiety circuits by serotonergic systems. *Stress* **8,** 233–246 (2005).

47. Commons, K. G. Two major network domains in the dorsal raphe nucleus: Two dorsal raphe networks. *Journal of Comparative Neurology* **523,** 1488–1504 (2015).

48. Muzerelle, A., Scotto-Lomassese, S., Bernard, J. F., Soiza-Reilly, M. & Gaspar, P. Conditional anterograde tracing reveals distinct targeting of individual serotonin cell groups (B5–B9) to the forebrain and brainstem. *Brain Structure and Function* **221,** 535–561 (2016).

49. Qi, J. *et al.* A glutamatergic reward input from the dorsal raphe to ventral tegmental area dopamine neurons. *Nature Communications* **5,** 5390 (2014).

50. Pollak Dorocic, I. *et al.* A Whole-Brain Atlas of Inputs to Serotonergic Neurons of the Dorsal and Median Raphe Nuclei. *Neuron* **83,** 663–678 (2014).

51. Ogawa, S. K., Cohen, J. Y., Hwang, D., Uchida, N. & Watabe-Uchida, M. Organization of Monosynaptic Inputs to the Serotonin and Dopamine Neuromodulatory Systems. *Cell Reports* **8,** 1105–1118 (2014).

52. Zhou, L. *et al.* Organization of Functional Long-Range Circuits Controlling the Activity of Serotonergic Neurons in the Dorsal Raphe Nucleus. *Cell Reports* **18,** 3018–3032 (2017).

53. Kim, J., Zhang, X., Muralidhar, S., LeBlanc, S. A. & Tonegawa, S. Basolateral to Central Amygdala Neural Circuits for Appetitive Behaviors. *Neuron* **93,** 1464–1479.e5 (2017).

54. Geddes, S. D. *et al.* Time-dependent modulation of glutamate synapses onto 5-HT neurons by antidepressant treatment. *Neuropharmacology* **95,** 130–143 (2015).

55. Wong-Lin, K., Wang, D.-H., Moustafa, A. A., Cohen, J. Y. & Nakamura, K. Toward a multiscale modeling framework for understanding serotonergic function. *Journal of Psychopharmacology* **31,** 1121–1136 (2017).

56. Wong-Lin, K., Joshi, A., Prasad, G. & McGinnity, T. M. Network properties of a computational model of the dorsal raphe nucleus. *Neural Networks* **32,** 15–25 (2012).

57. Tuckwell, H. C., Zhou, Y. & Penington, N. J. Simplified models of pacemaker spiking in raphe and locus coeruleus neurons. *arXiv:1508.05468 [q-bio].* arXiv: `1508.05468` (2015).

58. Tuckwell, H. C. & Penington, N. J. Computational modeling of spike generation in serotonergic neurons of the dorsal raphe nucleus. *Progress in Neurobiology* **118,** 59–101 (2014).

59. Marsat, G. & Maler, L. Neural Heterogeneity and Efficient Population Codes for Communication Signals. *Journal of Neurophysiology* **104,** 2543–2555 (2010).

60. Lapicque, L. Recherches quantitatives sur l'excitation électrique des nerfs traitée comme une polarisation. *Journal de Physiologie et de Pathologie Générale* **9,** 620–635 (1907).

61. Brunel, N. & van Rossum, M. C. W. Quantitative investigations of electrical nerve excitation treated as polarization: Louis Lapicque 1907. *Biological Cybernetics* **97,** 341–349 (2007).

62. Pillow, J. W. *et al.* Spatio-temporal correlations and visual signalling in a complete neuronal population. *Nature* **454,** 995–999 (2008).

63. Paninski, L. Maximum likelihood estimation of cascade point-process neural encoding models. *Network: Computation in Neural Systems* **15,** 243–262 (2004).

64. Truccolo, W., Eden, U. T., Fellows, M. R., Donoghue, J. P. & Brown, E. N. A Point Process Framework for Relating Neural Spiking Activity to Spiking History, Neural Ensemble, and Extrinsic Covariate Effects. *Journal of Neurophysiology* **93,** 1074–1089 (2005).

65. Pozzorini, C. *et al.* Automated High-Throughput Characterization of Single Neurons by Means of Simplified Spiking Models. *PLOS Computational Biology* **11** (ed Pillow, J. W.) e1004275 (2015).

66. Mensi, S. *et al.* Parameter extraction and classification of three cortical neuron types reveals two distinct adaptation mechanisms. *Journal of Neurophysiology* **107,** 1756–1775 (2012).

67. Mensi, S., Hagens, O., Gerstner, W. & Pozzorini, C. Enhanced Sensitivity to Rapid Input Fluctuations by Nonlinear Threshold Dynamics in Neocortical Pyramidal Neurons. *PLOS Computational Biology* **12** (ed Stevenson, I. H.) e1004761 (2016).

68. Naud, R., Gerhard, F., Mensi, S. & Gerstner, W. Improved Similarity Measures for Small Sets of Spike Trains. *Neural Computation* **23,** 3016–3069 (2011).

69. Crawford, L. K., Craige, C. P. & Beck, S. G. Increased Intrinsic Excitability of Lateral Wing Serotonin Neurons of the Dorsal Raphe: A Mechanism for Selective Activation in Stress Circuits. *Journal of Neurophysiology* **103,** 2652–2663 (2010).

70. Balachandar, A. & Prescott, S. A. Origin of heterogeneous spiking patterns from continuously distributed ion channel densities: a computational study in spinal dorsal horn neurons: Heterogeneous spiking patterns in spinal dorsal horn neurons. *The Journal of Physiology* **596,** 1681–1697 (2018).

71. Prescott, S. A., De Koninck, Y. & Sejnowski, T. J. Biophysical Basis for Three Distinct Dynamical Mechanisms of Action Potential Initiation. *PLoS Computational Biology* **4** (ed Graham, L. J.) e1000198 (2008).

72. Golowasch, J., Goldman, M. S., Abbott, L. F. & Marder, E. Failure of Averaging in the Construction of a Conductance-Based Neuron Model. *Journal of Neurophysiology* **87,** 1129–1131 (2002).

73. Connor, J. A. & Stevens, C. F. Voltage clamp studies of a transient outward membrane current in gastropod neural somata. *The Journal of Physiology* **213,** 21–30 (1971).

74. Jerng, H. H., Pfaffinger, P. J. & Covarrubias, M. Molecular physiology and modulation of somatodendritic A-type potassium channels. *Molecular and Cellular Neuroscience* **27,** 343–369 (2004).

75. Serôdio, P. & Rudy, B. Differential Expression of Kv4 K+ Channel Subunits Mediating Subthreshold Transient K+ (A-Type) Currents in Rat Brain. *Journal of Neurophysiology* **79,** 1081–1091 (1998).

76. Serodio, P., Kentros, C. & Rudy, B. Identification of molecular components of A-type channels activating at subthreshold potentials. *Journal of Neurophysiology* **72,** 1516–1529 (1994).

77. Aghajanian, G. Modulation of a transient outward current in serotonergic neurones by alpha1-adrenoceptors. *Nature* **315,** 501–503 (1985).

78. Segal, M. A potent transient outward current regulates excitability of dorsal raphe neurons. *Brain Research* **359,** 347–350 (1985).

79. Penington, N. J. & Tuckwell, H. C. Properties of IA in a neuron of the dorsal raphe nucleus. *Brain Research* **1449,** 60–68 (2012).

80. Getting, P. A. Mechanisms of pattern generation underlying swimming in Tritonia. III. Intrinsic and synaptic mechanisms for delayed excitation. *Journal of Neurophysiology* **49,** 1036–1050 (1983).

81. Berman, N. J. & Maler, L. Interaction of GABAB -Mediated Inhibition With Voltage-Gated Currents of Pyramidal Cells: Computational Mechanism of a Sensory Searchlight. *Journal of Neurophysiology* **80,** 3197–3213 (1998).

82. Mathieson, W. B. & Maler, L. Morphological and electrophysiological properties of a novel in vitro preparation: the electrosensory lateral line lobe brain slice. *Journal of Comparative Physiology A* **163,** 489–506 (1988).

83. McCormick, D. A. Functional properties of a slowly inactivating potassium current in guinea pig dorsal lateral geniculate relay neurons. *Journal of Neurophysiology* **66,** 1176–1189 (1991).

84. Locke, R. E. & Nerbonne, J. M. Role of Voltage-Gated K+ Currents in Mediating the Regular-Spiking Phenotype of Callosal-Projecting Rat Visual Cortical Neurons. *Journal of Neurophysiology* **78,** 2321–2335 (1997).

85. Doiron, B., Longtin, A., Turner, R. W. & Maler, L. Model of Gamma Frequency Burst Discharge Generated by Conditional Backpropagation. *Journal of Neurophysiology* **86,** 1523–1545 (2001).

86. Li, J., Bickford, M. E. & Guido, W. Distinct Firing Properties of Higher Order Thalamic Relay Neurons. *Journal of Neurophysiology* **90,** 291–299 (2003).

87. Cudmore, R. H., Fronzaroli-Molinieres, L., Giraud, P. & Debanne, D. Spike-Time Precision and Network Synchrony Are Controlled by the Homeostatic Regulation of the D-Type Potassium Current. *Journal of Neuroscience* **30,** 12885–12895 (2010).

88. Lein, E. S. *et al.* Genome-wide atlas of gene expression in the adult mouse brain. *Nature* **445,** 168–176 (2007).

89. Caporale, N. & Dan, Y. Spike Timing–Dependent Plasticity: A Hebbian Learning Rule. *Annual Review of Neuroscience* **31,** 25–46 (2008).

90. Haj-Dahmane, S., Béïque, J. C. & Shen, R.-Y. GluA2-Lacking AMPA Receptors and Nitric Oxide Signaling Gate Spike-Timing–Dependent Potentiation of Glutamate Synapses in the Dorsal Raphe Nucleus. *eNeuro* **4,** e0116–17.2017 (2017).

91. Suzuki, S. & Rogawski, M. A. T-type calcium channels mediate the transition between tonic and phasic firing in thalamic neurons. *Proceedings of the National Academy of Sciences* **86,** 7228–7232 (1989).

92. Burlhis, T. M. & Aghajanian, G. K. Pacemaker potentials of serotonergic dorsal raphe neurons: Contribution of a low-threshold Ca2+ conductance. *Synapse* **1,** 582–588 (1987).

93. Milescu, L. S., Yamanishi, T., Ptak, K. & Smith, J. C. Kinetic Properties and Functional Dynamics of Sodium Channels during Repetitive Spiking in a Slow Pacemaker Neuron. *Journal of Neuroscience* **30,** 12113–12127 (2010).

A Supplementary figures

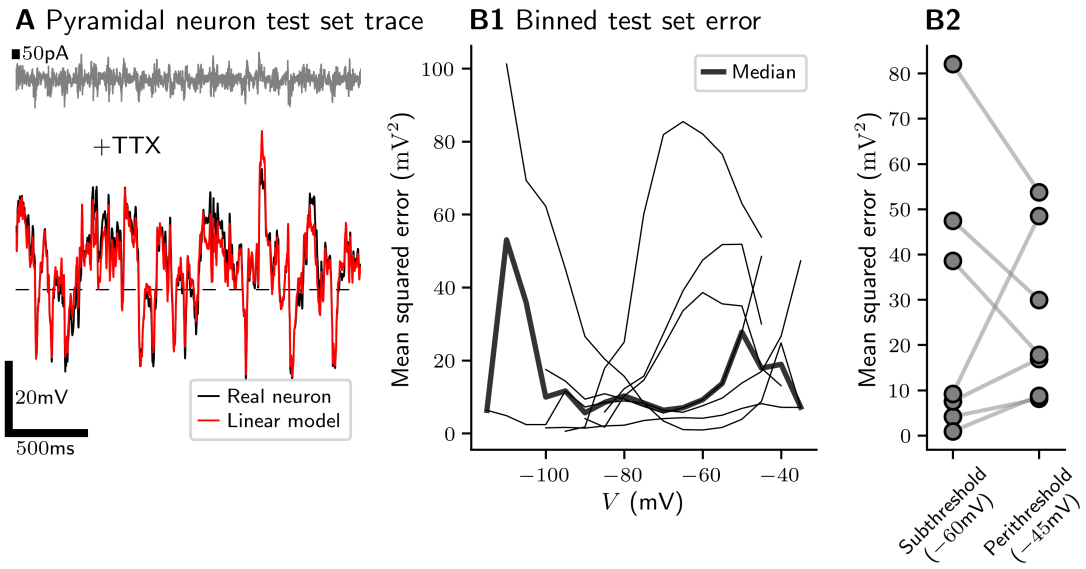

Figure S1: Linear subthreshold model accurately describes pyramidal neurons. *A*. Sample test data from a pyramidal neuron in TTX and corresponding model prediction. *B*. Linear model performance quantified as a function of voltage. *B1*. Model error binned according to the voltage of the real neuron. Fine lines are individual neurons and bold indicates the median. *B2*. Model performs similarly at rest and near spike threshold ($N = 7$). Gray lines indicate paired data taken from one neuron. Data collected by Chloe Stewart and Dominic Cyr.

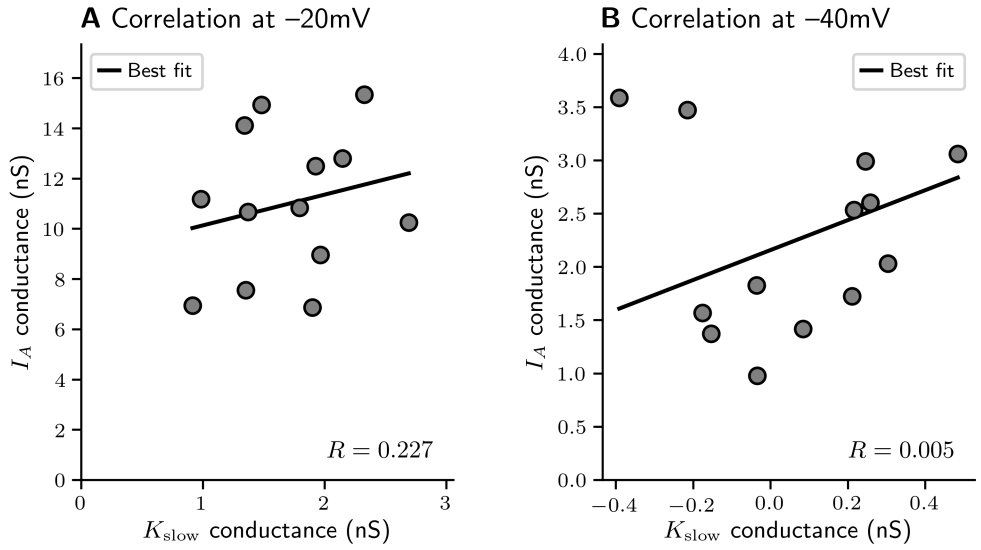

Figure S2: I_A and K_{slow} magnitudes are uncorrelated. Pearson correlation coefficient R is indicated on each plot. Each dot is one neuron ($N = 13$). *A*. Correlation plot using conductance at -20 mV as a reference value. *B*. Correlation plot using conductance at -40 mV as a reference value.

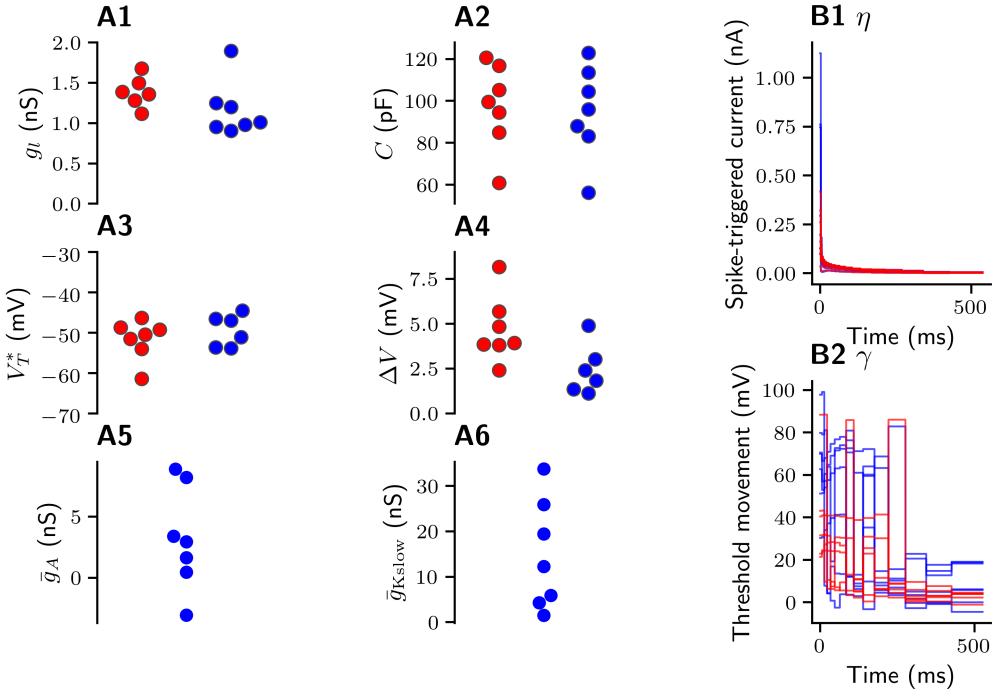

Figure S3: GIF (red) and KGIF (blue) parameter values from 5HT neuron fits. *A*. Passive membrane and firing mechanism parameters. *B*. Spike-triggered filters. See [65].

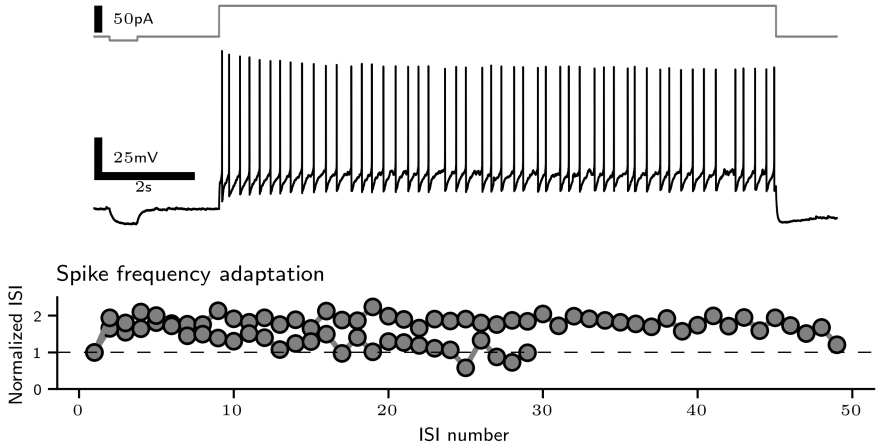

Figure S4: Spike frequency adaptation in 5HT neurons in response to a 15 s current step. Sample trace (top) and normalized inter-spike-interval (ISI) length (bottom; each line is one cell).

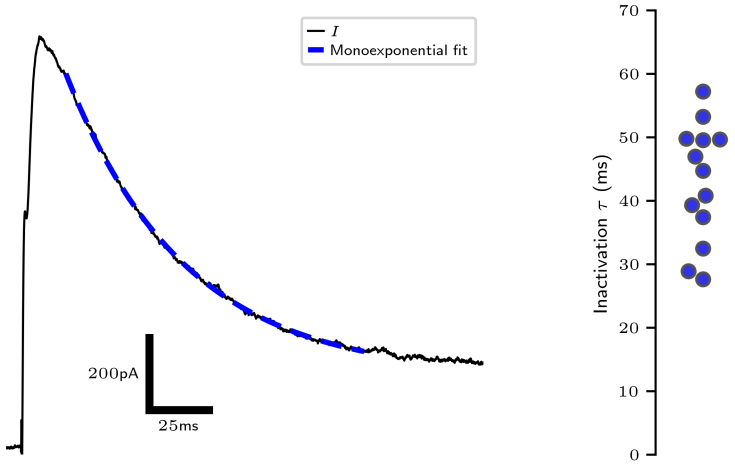

Figure S5: Decay time constant of I_A in 5HT neurons during a -90 mV to -20 mV step. Sample trace with monoexponential fit (left) and distribution of τ_h fits (right). τ_h distribution 42.9 ± 9.0 mV (mean±SD).

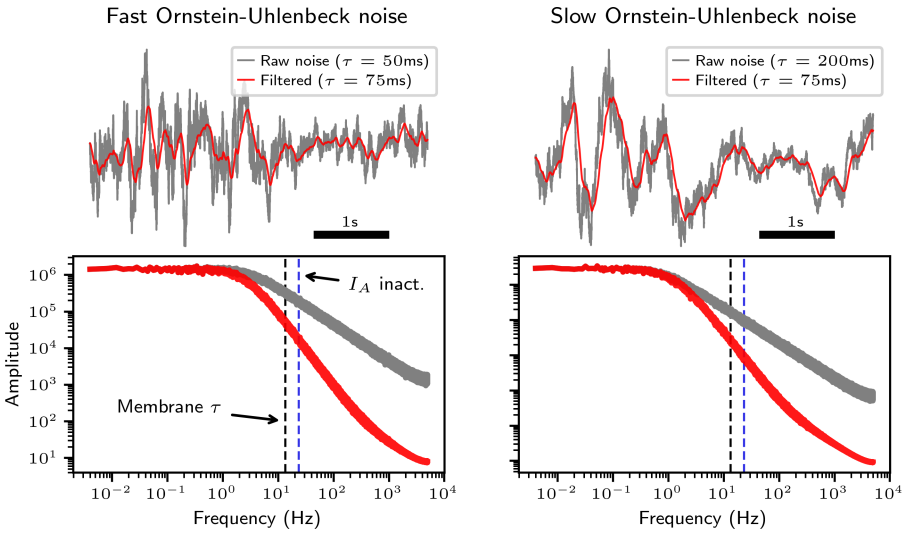

Figure S6: Frequency content of Ornstein-Uhlenbeck noise used in this work. Sample traces (top) before (gray) and after (red) filtering by a simulated neuron with a membrane time constant of 75 ms. Frequency content (bottom) before (gray) and after (red) filtering by the same simulated neuron as at top. Critical frequencies of the membrane filter (using $\tau_{\text{mem}} = 75\,\text{ms}$) and I_A lowpass filter (using $\tau_h = 42.9\,\text{ms}$, the mean value from fig. S5) are indicated with dashed lines.